Accepted for publication in Antioxidants & Redox Signaling. DOI: 10.1089/ars.2017.7341

Forum review

In vivo Application of Proton Electron Double Resonance Imaging.

Shun Kishimoto[1], Murali K. Cherukuri[1], Valery V. Khramtsov[2], Hideo Utsumi[3], David J. Lurie[4]

[1]Radiation Biology Branch, Center for Cancer Research, National Cancer Institute, Bethesda, MD 20892

[2] In Vivo Multifunctional Magnetic Resonance center and Department of Biochemistry, Robert C. Byrd Health Sciences Center, West Virginia University, Morgantown, West Virginia 26506,

[3] School of Pharmaceutical Sciences, The University of Shizuoka, Yada, Suruga-ku, Shizuoka 422-8526, Japan.

[4] Aberdeen Biomedical Imaging Centre, School of Medicine, Medical Sciences & Nutrition, University of Aberdeen, Aberdeen AB25 2ZD, United Kingdom.

Word Count:	7558
Reference Number:	137
Number of gray scale illustrations:	11
Number of color illustrations:	7 (color in online only)

Address Correspondence to: David J. Lurie, PhD.
Aberdeen Biomedical Imaging Centre, School of Medicine, Medical Sciences & Nutrition, University of Aberdeen, Aberdeen AB25 2ZD, United Kingdom.
Phone: +44 1224 554061
Fax: +44 1224 552514
Email: d.lurie@abdn.ac.uk

Manuscript Key-words: Overhauser MRI, OMRI, PEDRI, Free radical, imaging

Abstract:

Significance:

Proton-electron double resonance imaging (PEDRI) is a double resonance imaging method that employs electron paramagnetic resonance irradiation prior to low field magnetic resonance imaging (MRI) so that the polarization of the electron spin will be transferred to nearby protons, resulting in higher proton signal. The enhanced MRI signal from local areas where exogenously administered radicals distribute provides information about the local microenvironment such as pO_2, tissue permeability, redox status, and acid-base balance.

Recent Advances:

Local acid-base balance can be imaged by taking advantage of the different resonance frequency of radical probes between R and RH^+ forms. The redox status can also be imaged using the loss of radical-related signal after reduction of radical probes. Unlike previous proton-electron double resonance imaging techniques using stable single-line radicals, these imaging methods require specific radicals and pulse sequences that are optimized for specific studies.

Critical Issues:

High radiofrequency (RF) irradiation power is needed for high enhancement of the proton MRI signal, which may possibly be harmful to living tissue by unwanted heat deposition. Free radical probes differ depending on the purpose of PEDRI. Some probes are less effective for enhancing signal than others, which can reduce image quality. It is so far not possible to image endogenous radicals by PEDRI because low concentrations and broad line widths of the intrinsic radicals lead to negligible signal enhancement.

Future Directions:

PEDRI has similarities with electron paramagnetic resonance imaging (EPRI) because they both observe the EPR signal; directly in the case of EPRI and indirectly with PEDRI. PEDRI images provide information vital to research on homeostasis, development of diseases or treatment responses in vivo. It is expected that the development of new EPR techniques will give insights into new PEDRI applications and vice versa.

Introduction:

Proton-electron double resonance imaging (PEDRI), also known as Overhauser-enhanced magnetic resonance imaging (OMRI), is an imaging modality with similarities to MRI as well as to Electron Paramagnetic Resonance Imaging (EPRI). It is normally carried out at extremely low magnetic fields of 10-40 mT corresponding to proton Larmor frequencies of 0.5 -2 MHz and electron Larmor frequencies of 300 – 1200 MHz. At such low magnetic fields, the polarization of the ^{1}H spin states is small, making it difficult to generate MR images with useful signal-to-noise ratio (SNR). However, in the presence of paramagnetic species with narrow EPR resonances, application of electromagnetic radiation at the resonance frequency of the electron spins (typically at radiofrequency) significantly enhances the nuclear polarization to a theoretical maximum of 330-fold (half of $\gamma e/\gamma p = 659$), where γe and γp are respectively the electron and proton gyromagnetic ratios. Under these circumstances, due to dipolar coupling between the unpaired electrons and the solute (water) protons in the system, polarization is transferred to nearby protons creating much larger population differences between the nuclear spin states, in turn leading to a large increase in signal intensity (48, 49, 79, 114). This method is known as the Overhauser effect, or sometimes as liquid-state Dynamic Nuclear Polarization (DNP). The saturation of electrons is carried out for a duration in the order of the proton spin lattice relaxation time after which the ç detection and spatial encoding follow immediately, resulting in a significant enhancement of the proton signals. Images with useful SNR can be acquired in such manner even at such low magnetic fields. Furthermore, PEDRI is effectively an indirect form of EPRI in the sense that the enhancement of proton signals is proportional to the concentration of the paramagnetic system and the degree of saturation of the EPR system. In a PEDRI image, regions of the sample containing free radicals “light up” due to the Overhauser-enhanced proton nuclear magnetic resonance (NMR) signal, revealing the location of the free radical. This review covers the topic of PEDRI from the historical background to various preclinical applications of the technique, including pO_2 mapping, permeability mapping, redox mapping and pH mapping.

Historical background:

Dynamic nuclear polarization of nuclear spin states was predicted by Albert Overhauser in 1953 (100), a technique which became known as the Overhauser effect. In the theory, saturating the electron spin resonance of a paramagnetic species will significantly enhance the polarization of surrounding nuclear spins. This prediction was confirmed by Carver and Slichter in 1956 who had been researching the electron spin resonance of lithium (20). In

the process of experimental verification of the Overhauser effect, they concluded that the effect could be observed in any system in which the nuclear relaxation was dominated by a coupling to electrons in which the nuclear spin flip requires a simultaneous electron flip. To further verify these conclusions, they successfully performed experiments on systems of ^{7}Li, ^{23}Na and even ^{1}H (20). The Nuclear Overhauser Effect (NOE) is an extension of the Overhauser effect explained with experimental observation by Kaiser in 1962, demonstrating polarization transfer from one population of nuclear spins to another via cross relaxation (65). The NOE is utilized in the field of NMR spectroscopy, including its use to determine the three-dimensional structure of complex molecules. Here, we focus on the Overhauser effect where electron spin polarization is transferred to ^{1}H polarization with subsequent MRI to reveal the localized concentration of free radicals.

The ability to image the distribution of paramagnetic solutions in vivo has many potential uses in biology and medicine. EPRI, which uses methods analogous to those employed in NMR imaging has been developed with considerable effort (8, 9, 31, 38, 85). However, EPR was typically restricted to small samples (~50 mm) because of the relatively large line widths (~MHz) and the strong gradients necessary to achieve useful spatial resolution. Endogenous free radicals are present in small quantities and are often short-lived with very low steady-state concentration. Therefore, it is necessary to introduce free radicals as "probes" into the living system which should be biocompatible, stable during the measurement and non-toxic. Oxygen concentration in tissues can be deduced via its line broadening effect on the EPR spectrum of injected free radical.

To image paramagnetic species such as injected free radicals in larger-sized biological systems and animals, Lurie et al. developed in 1988 an imaging technique that combines proton NMR imaging with the Overhauser effect, called Proton electron double resonance imaging (PEDRI), which is also known as Overhauser-enhanced magnetic resonance imaging (OMRI) (79). The main difference between PEDRI and EPRI is that the enhanced proton signal is observed in PEDRI, while the electron signal from the free radical probe is observed directly in EPRI. Unlike EPRI, large sample sizes with higher resolution can be achieved in PEDRI because proton resonances are detected after enhancement by the Overhauser effect. The terms PEDRI and OMRI represent one and the same technique; throughout this article, we will use PEDRI.

Under appropriate conditions, EPR irradiation causes a transfer of polarization from the unpaired electrons to the proton nuclei of tissue water, increasing the intensity of the ^{1}H NMR signal. The enhancement of the NMR signal can be described by the enhancement factor, E, given by

$E = A_Z / A_0$ [1]

where A_Z and A_0 are the NMR signals with and without EPR irradiation, respectively. The enhancement can be described by the following relationship:

$E = 1-\rho f\,(s/n)(\gamma e/\gamma p)$ [2]

where ρ is the coupling factor ($-1 \le \rho \le 1/2$, with $\rho = 1/2$ for dipole–dipole interactions), f is the leakage factor ($0 \le f \le 1$), s is the saturation factor ($0 \le s \le 1$), n is the number of hyperfine lines in the EPR spectrum (n = 3 for a typical nitroxide free radical) and γe and γp are the electron and nuclear gyromagnetic ratios (for experiments involving protons, the ratio ($\gamma e/\gamma p \approx 659$). Equation [2] assumes that only one EPR resonance is irradiated at a time (83).

Fig. 1 shows the capability of PEDRI to provide ^1H images at low magnetic fields and to assess the influence of dissolved oxygen on the enhancement (79). Two identical phantom tubes were filled with 2.5 mM 4-hydroxy-2,2,6,6-tetramethylpiperidine-1-oxyl (TEMPOL) solution dissolved in water, one of which had been equilibrated with nitrogen by bubbling the gas through the phantom and the other with air. The nitrogen-equilibrated phantom exhibited a 40% greater enhancement than the air-equilibrated one with calculated enhancement factors of -6.9 (left) and -9.8 (right). This effect occurs because EPR resonances of spin labels are differentially broadened in the presence of dissolved oxygen (13, 46, 100, 117). A broad EPR line is more difficult to saturate, thus the observed enhancement factor for a given magnetic field strength is reduced. PEDRI images have been obtained with TEMPOL concentrations as low as 0.3 mM, which is nevertheless more than three orders of magnitude higher than the concentration of intrinsic radicals (84).

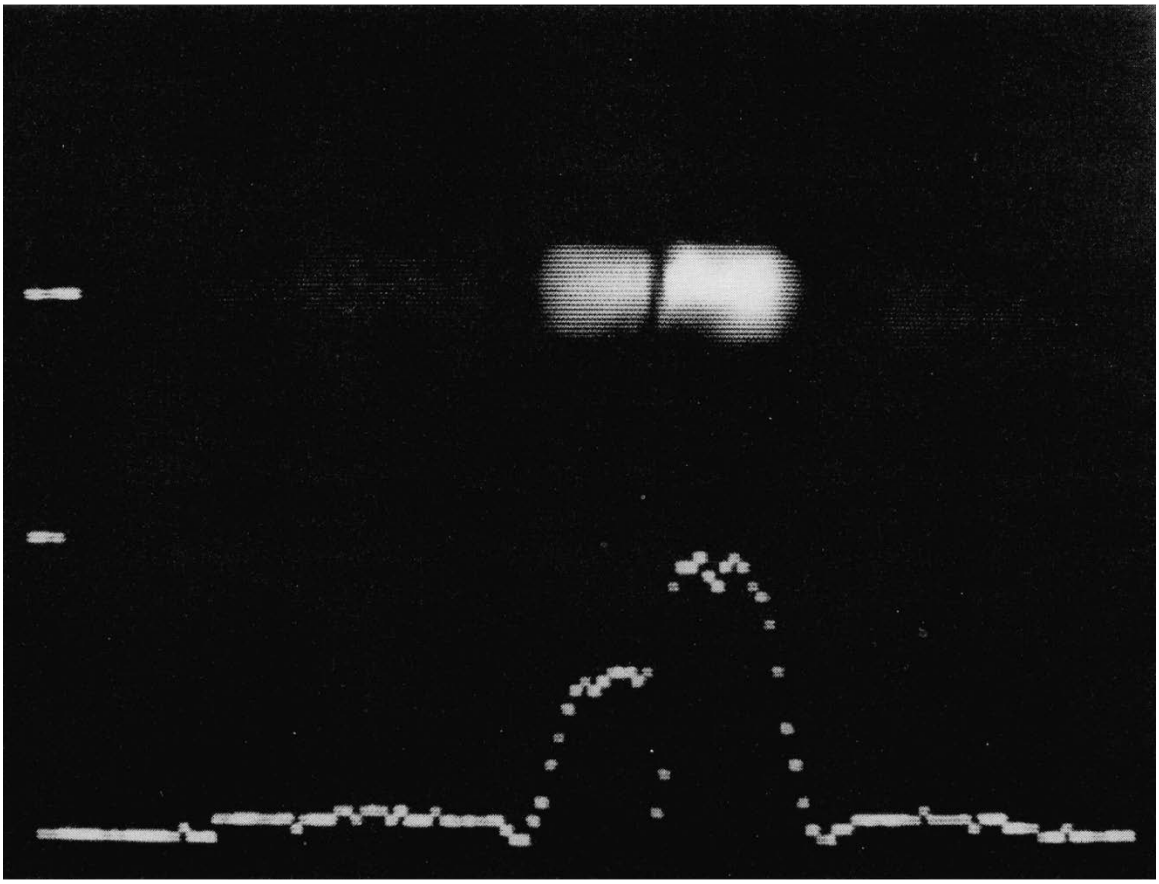

Figure 1

Fig 1 shows a PEDRI magnitude image of two phantom tubes containing air-equilibrated (left) and nitrogen-equilibrated (right) 2.5 mM 4-hydroxy-2,2,6,6-tetramethylpiperidine-1-oxyl (TEMPOL) solution dissolved in water (79). Due to different oxygen concentration, the magnitude of enhancement is higher in right phantom tube. Calculated enhancement factors were -6.9 (left) and -9.8 (right). Reprinted by permission from Lurie et al., J.Magn.Reson. 76, 366-370 (1988) (ref. (79)).

Field cycling:

In order to make PEDRI applicable for in vivo experiments by avoiding excessive sample heating due to high power of EPR irradiation, field cycling (FC) was introduced in the pulse sequence of image acquisition, which greatly reduces the applied field strength during EPR irradiation (81). In FC-PEDRI, the magnetic field applied to the sample is changed throughout the experiment. Scheme 1 shows the pulse sequence of FC-PEDRI. The EPR irradiation is applied at low magnetic field strength (at correspondingly low frequency), during which the Overhauser polarization transfer alters the proton magnetization (Evolution Period). The magnetic field is then increased rapidly for the detection period, during which the NMR detection pulse(s) and magnetic field gradients are applied (Detection Period).

Applying the EPR irradiation at low field decreases the EPR frequency and the non-resonant power deposition (which varies approximately as the square of the frequency), allowing larger samples to be used. The optimum EPR frequency as well as evolution field depends on the EPR linewidth of the free radical and on the size of the sample. It has previously been shown that with nitroxide free radicals and large samples, the optimum frequency is between 30 and 60 MHz, corresponding to an Evolution (EPR) field of ~3 mT (78). Detecting the NMR signals at high field is necessary to increase the SNR of the experiment.

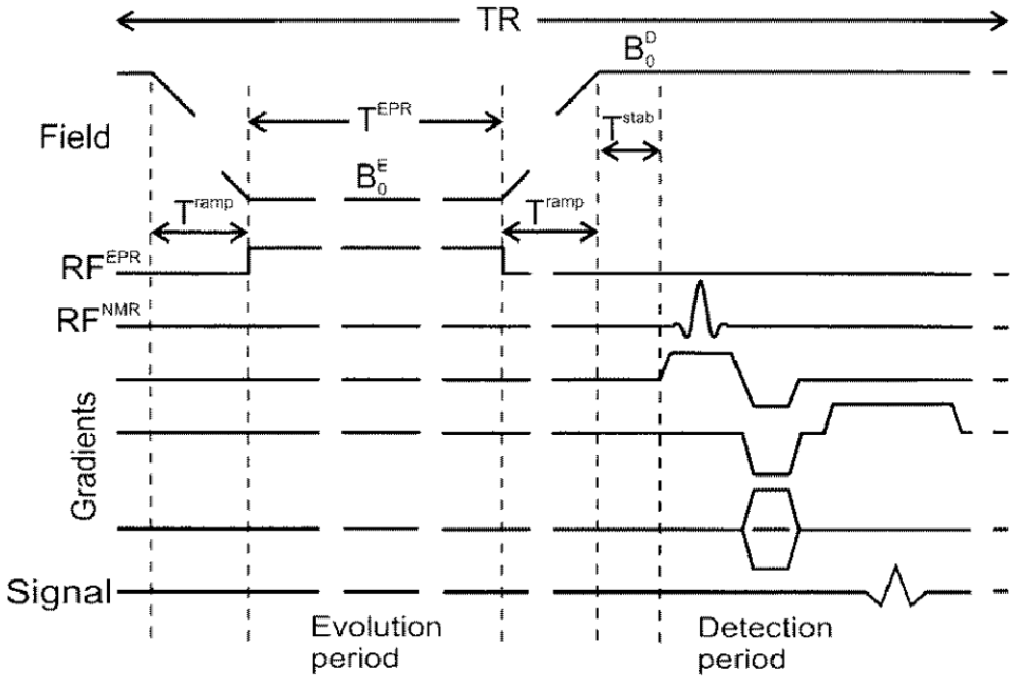

Scheme. 1

FC-PEDRI pulse sequence, showing magnetic field, field gradient and waveforms. Reprinted by permission of IOP Publishing from Lurie et al., Phys.Med.Biol., 43, 1877-86 (1998) (ref. (83)).

Fig. 2 shows FC-PEDRI images of a resolution phantom (B, C and D); a field-cycled non-PEDRI image (A) is also shown for comparison (81). The center of the phantom consisted of five tubes of internal diameters 15, 9, 5, 4, and 3 mm filled with 2 mM TEMPOL solution. These were enclosed in a cylindrical container of diameter 4 cm which was filled with water doped with copper sulfate to give the same T_1 as that of the free radical solution (650 ms at 2.5 MHz).

14 sample tubes with internal diameters of 8 mm were attached around the outside of the cylinder, alternate tubes being filled with 2 mM TEMPOL solution or copper sulfate-doped water. The overall diameter of the phantom was 6 cm, about the size of a small rat. The three FC-PEDRI images were obtained using EPR irradiation time (T^{EPR}) values of 750, 1000, and 1500 ms with a repetition time (TR) of 2000 ms, and the average observed enhancement factors were -4.0, -5.3, and -7.1, respectively. The instantaneous power level in the EPR irradiation was approximately 7 W/kg, while the average applied power ranged from 2.7 to 5.3 W/kg depending on the pulse sequence timing. In FC-PEDRI, the enhanced versus unenhanced image intensity ratio depends not only on the power of the EPR irradiation but also on the relative timing of the polarization and evolution intervals, and the values of B_0^P and B_0^D. At the beginning of the evolution period, the size of the magnetization depends on the length of the polarization period compared with the sample's T_1 at B_0^P. During the evolution period, the magnetization decays at a rate determined by the sample's T_1 at B_0^E. Meanwhile the magnetization in regions of the sample containing free radical increases at a rate depending on T_1 toward an equilibrium value which depends on the EPR irradiation power. The results from FC-PEDRI show that free radicals can be imaged with greater resolution than with EPR, which typically relies on projection reconstruction.

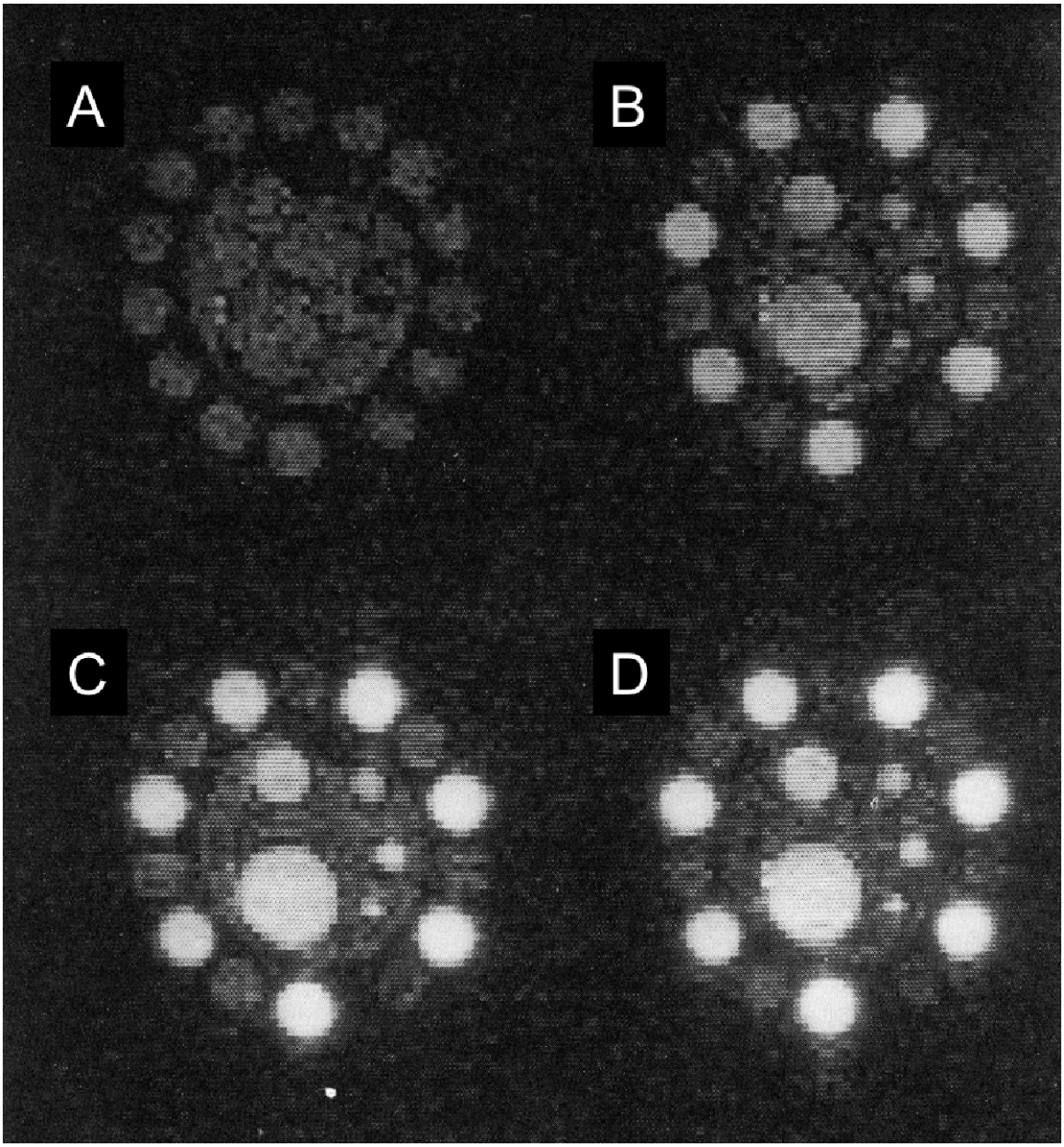

Figure 2

Images of phantom containing 2 mM TEMPOL solution and copper sulfate-doped water. Images are 64 X 64 sections of original 128 x 128 images, which had 15 cm field of view, 15 mm slice thickness. All images are field-cycled, with $B_0^P = B_0^D = 0.01$ T, $B_0^E = 0.005$ 1 T, saturation-recovery NMR sequence with TR = 2000 ms, four averages. Image (**A**) has $T^{EPR} = 1000$ ms, no EPR irradiation. Images **B-D** have EPR irradiation at 160 MHz, power 1 W. Image (**B**) has $T^{EPR} = 750$ ms; observed enhancement factor E = -4.0. Image (**C**) has $T^{EPR} = 1000$ ms; E = -5.3. Image (**D**) has $T^{EPR} = 1500$ ms; E = -7. I. Reprinted by permission from Lurie et al., J.Magn.Reson., 84, 431-437 (1989) (ref. (81)).

In vivo experiments using FC-PEDRI have been reported. Fig. 3 shows images from an in vivo experiment using the nitroxide radical proxyl carboxylic acid (PCA) in the rabbit (83). An anaesthetized rabbit was placed supine with the

kidneys placed centrally and an FC-PEDRI image was collected. The free radical probe was then administered, and a series of FC-PEDRI images was obtained at approximately 6 min intervals. Images were obtained using both 64 × 64 and 128 × 128 matrices. In both cases the image parameters were: field of view 15 cm, slice thickness 3 cm, TR = 1000 ms, T^{EPR} = 300 ms, T^{ramp} = 40 ms, T^{stab} = 10 ms, EPR frequency 51.0 MHz, B_0^E = 3.05 mT. The forward power to the birdcage resonator was approximately 300 W, and the power absorbed in the animal can be estimated as 130 W using the loaded and unloaded Q factors (measured to be 193 and 346 respectively). Considering the duty cycle of the EPR irradiation (300 ms in 2000 ms, or 15%), the average specific absorption rate (SAR) in the 2.2 kg animal is 9 Wkg^{-1}. Considering the delays between consecutive image collections, the overall SAR was only 3 W kg^{-1}. Although this is still higher than desirable, the experiment successfully demonstrated that FC-PEDRI of a moderately-large animal was possible without overheating the animal due to non-resonant absorption of the EPR irradiation. Fig.3 shows 'without EPR', 'with EPR' and 'difference' transaxial images through the animal's abdomen obtained 2 min after injection of the nitroxide free radical. As reported in the rat (111), PCA is cleared through the rabbit's kidneys, and this can be seen clearly in the difference image, together with major blood vessels. The signal-to-noise ratio in the difference image was measured to be 14±1.5 (83).

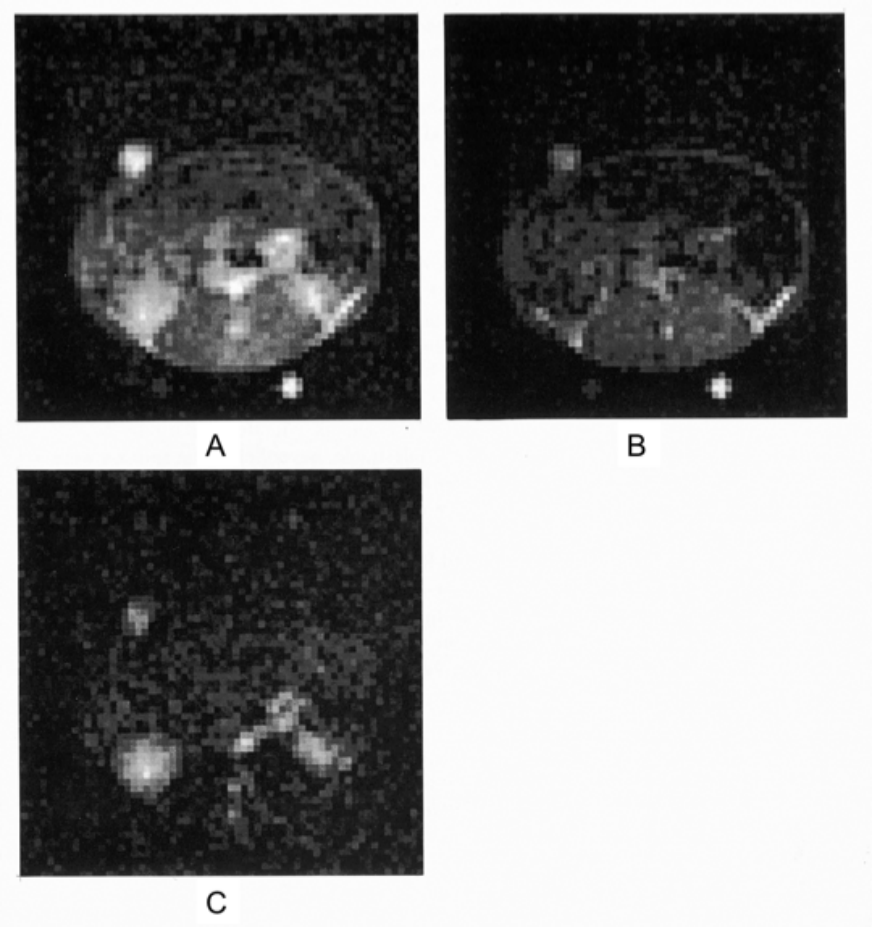

Figure 3.

Trans-axial images through abdomen of anaesthetized rabbit following injection of PCA nitroxide free radical: (**A**) 'without EPR' image, (**B**) 'with EPR' image, (**C**) 'difference' image. The difference image shows the animal's kidneys and major blood vessels. The high- intensity region above the animal is a reference vial containing 1 mM PCA solution. Vials containing CuSO4 solution are seen below the animal in (a) and (b); these are used to aid positioning. Reprinted by permission of IOP Publishing from Lurie et al., Phys.Med.Biol., 43, 1877-86 (1998) (ref. (83)).

Optimization of probes for PEDRI:

The feasibility of in vivo application of PEDRI had been intensively researched by several groups in the literature in 1990s. However, nitroxides used as contrast media in the studies until the late 1990s were not optimized enough to produce morphological images at ~10 mT (3, 47, 79, 81). The nitrogen nucleus has a spin 1 and splits the

single transition into three transitions. So, when one transition is irradiated, only 1/3 of the possible enhancement is available and high power was needed to saturate it due to the short relaxation time. Both these factors result in restricted enhancement and consequently a low SNR in the resulting images. In addition, the short pharmacological half-lives of these species further limited their use for PEDRI research. To improve the SNR of in vivo PEDRI, triarylmethyl or trityl radicals (TAM), paramagnetic substances with single narrow lines and long relaxation time were synthesized as probes (4, 17, 44, 105, 131, 134). Scheme 2A shows the chemical structural formula of TAM and Scheme 2B illustrates the case of Φ when it is Ox63. The narrow line without splitting was realized by designing the location of unpaired electron more than five bonds away from magnetic nuclei. The carboxyl group in Φ makes TAM highly soluble. TAM distributes in extracellular space due to its negative charge. TAM also has other characteristics needed for EPR probe (stability, low toxicity, long in vivo half-lives and pO_2 dependent EPR line widths).

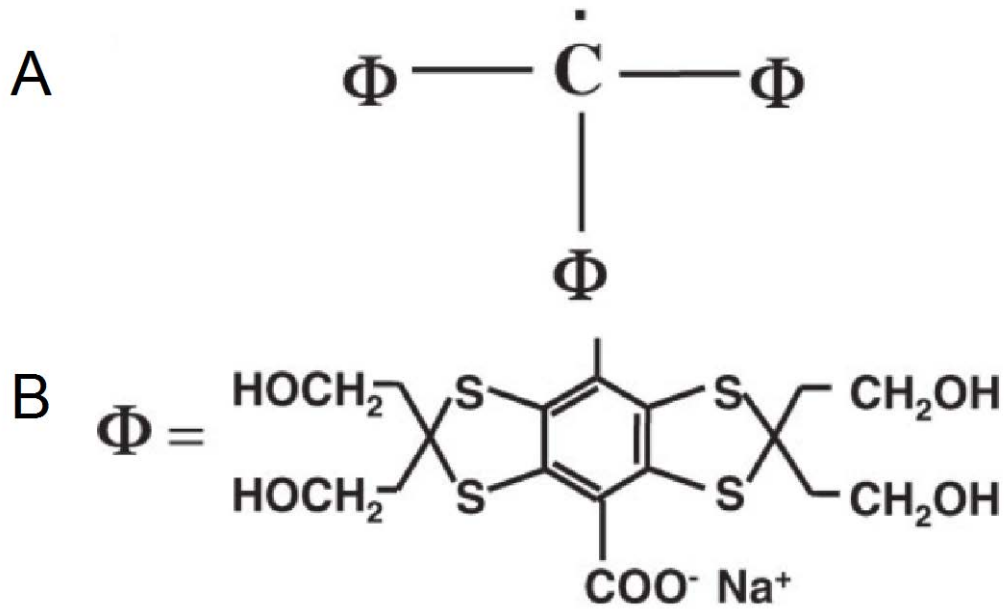

Scheme 2 Chemical structure of TAM. . Reprinted by permission from Krishna et al., Proc.Natl.Acad.Sci.USA 99, 2216-21 (2002) (ref. (75)).

By combining these probes with improved imaging hardware and pulse sequences, significant improvements in the quality of morphological images in rats were reported in 1998 (44). That study also showed that TAM behaved

pharmacokinetically as an extra-vascular, extra-cellular MR contrast medium, which indicated that it remains mainly within the vascular bed during the first few re-circulations in the body. In vivo images from another study are illustrated in Fig. 4, which shows the difference between unenhanced MRI and PEDRI using TAM in a mouse at 20 mT. The PEDRI image displays significantly higher SNR, though both images were taken in comparable times. The imaging parameters are listed in the figure caption(82).

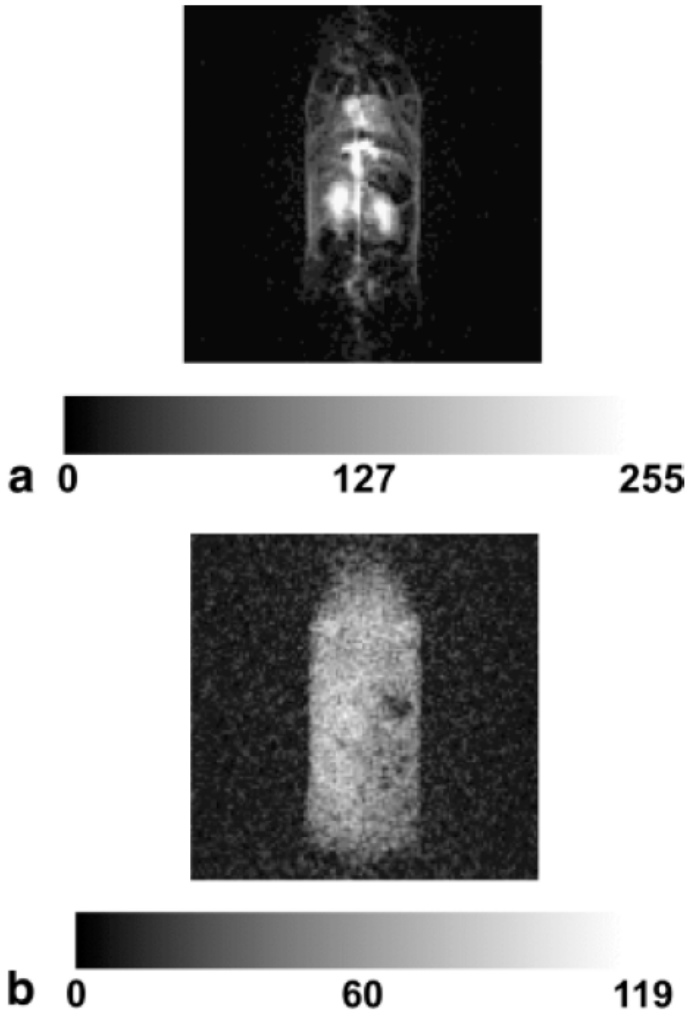

Figure 4

a: Projective coronal gradient-echo PEDRI image of an anesthetized 30-g mouse 3 min after administration of i.v. dose of 0.66 mmol/kg TAM. Image shows an enhancement of –5 in the kidneys and major blood vessels. Image parameters: matrix size 128 x 128; FOV 8 x 8 cm; TR 1200 ms; TE 12 ms; TEPR 400 ms; NEX 1; EPR irradiation at 564 MHz. The applied EPR irradiation power at the resonator was 3 W with 26% absorbed

by the 30-gm mouse, resulting in an SAR of 7.4 W/kg during the 2-min 40-s acquisition time. b: Image of the same animal without EPR irradiation (other parameters are identical). Reprinted by permission from Lurie et al., Magn.Reson.Med. 47, 181-186 (2002) (ref. (82)).

Fig. 5 also shows a set of coronal FC-PEDRI images (EPR-on, EPR-off and difference, Fig. 5A, 5B and 5C respectively) of a 172 g rat, 51 min after injection of a dose of TAM; imaging parameters are listed in the figure caption (80). These images illustrate the advantage of using a relatively high detection magnetic field (0.45 T) in order to boost the overall SNR, with attendant increase in sensitivity and image quality. A slice thickness of 30 mm was used to visualize the injected free radicals independent of its anterior– posterior position within the animal. In the difference image, the animal's kidneys and bladder can clearly be seen. The ureters are also clearly visible, even though they represent only a small fraction of the volume of a voxel (the voxel dimensions are 30/0.8/0.8 mm). It is also noteworthy that by using TAM the imaging of renal excretion has improved substantially from Fig. 3 using PCA.

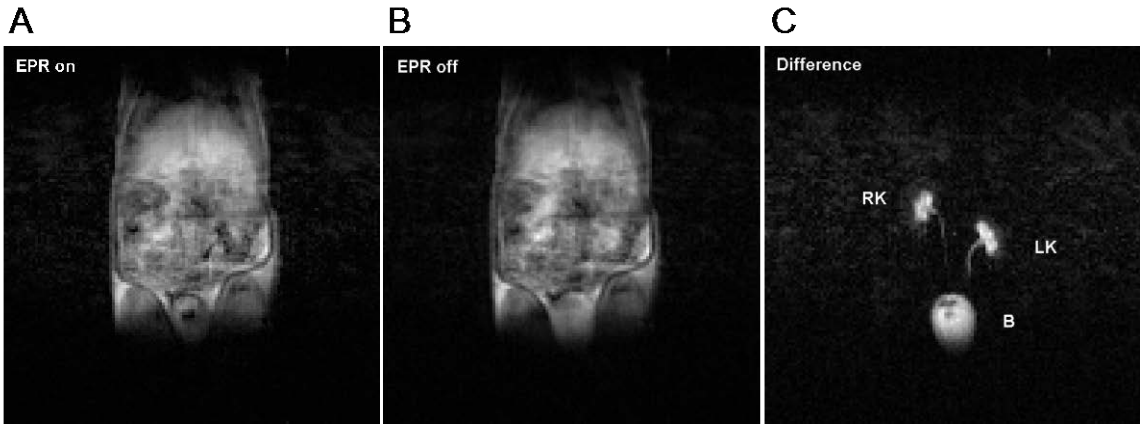

Figure 5

Images of 172 g anesthetized rat, 51 min after injection of 0.58 mmol/kg iv dose of TAM. (**A**) Image acquired with EPR irradiation; (**B**) image acquired without EPR irradiation; (**C**) difference image; labels: RK—right kidney, LK—left kidney, B—bladder. Acquisition parameters: 128 x 128 matrix; field of view, 100 x 100 mm; slice thickness, 30 mm; NEX 1; TR, 1050 ms; T^{EPR}, 400 ms; B_0^E, 3.30 mT; EPR irradiation, 93.1 MHz, 15 W applied power. Reprinted by permission from Lurie et al., Magn.Reson.Imaging 23, 175-181 (2005) (ref. (80)).

pO_2 mapping with PEDRI:

Oxygen supply and diffusion into tissues is necessary for cellular function (19). The oxygen pO_2, which is a key measure of the physiological state of an organ, results from the balance between oxygen delivery and its consumption. Oxygen transported by red blood cells is delivered dependent on the metabolic requirements and

functional status of each organ. Tissue oxygenation is severely disturbed during pathological conditions such as cancer, diabetes, coronary heart disease, stroke, etc., which are associated with decrease in pO_2 (19). Several different techniques have been developed to quantify the concentration of oxygen. Invasive methods involve oxygen sensitive electrodes such as the Clark electrode (51, 54) or the Eppendorf electrode (127, 130). As non-invasive methods, the blood oxygenation level dependent (BOLD) MRI techniques (16, 96, 99) where a T_2* sensitive gradient echo pulse sequences is used to visualize the ratio between oxy/deoxy-hemoglobin or non-hydrogen nuclei such as ^{17}O (89, 97, 136) or ^{19}F MR images (88, 101, 107) where the oxygen concentration is reflected in the signal intensity of the image are available.

The electron spin relaxation times are mainly determined by self-broadening and oxygen-induced relaxation (1, 35, 39, 40, 67, 118, 120, 137). In PEDRI the presence of O_2 shortens the relaxation times and consequently results in the decreased transfer of polarization to nuclear spins during the EPR irradiation. Variations in the concentration of the unpaired electron substance can also influence the electron spin relaxation times in the same way. Hence, the signal intensity of PEDRI can be calculated using both oxygen concentration and concentration of radical probe on the relaxation rates. Thus, in vivo oximetry is one of the most straightforward and useful applications of PEDRI (4, 33, 75, 79, 93). EPR methods (both spectroscopic and imaging) are also employed to obtain oxygen information. In EPRI, the spatial as well as the spectral information of the exogenously administered spin probes is obtained. Therefore, EPRI present the in vivo visualization of the spin probes but without complementary anatomical information. In contrast, MRI is a well-established modality that gives superior anatomical information. PEDRI uses the Overhauser effect, and thereby indirectly detects the EPR-signal. After the EPR irradiation, using standard MR-imaging techniques, distribution of the probe and the oxygen concentration near the probe is visualized in PEDRI (4, 45, 117, 128). In vivo applications of PEDRI oximetry have been demonstrated, for example by Golman et al. (45).

In the oncology field, approximately one-third of human tumors evaluated for oxygen status have shown significant oxygen deficiency. Oxygen deficiency increases the tumor's resistance toward cancer treatment modalities, including radiation and chemotherapy (25, 52, 53, 55, 104, 115, 126). Additionally, hypoxic microenvironments in tumors are known to promote processes driving malignant progression, such as angiogenesis, elimination of p53 tumor suppressor activity, genetic instability, and metastasis (42, 52, 94). Understanding of tumor hypoxia could lead to the discovery of diagnostic and prognostic markers for malignant progression, discovery of novel therapeutic targets, and the development of new constructs for gene therapy applications in human cancer. Therefore, oximetry by PEDRI,

which is a non-invasive and real-time measurement, is of importance in preclinical research. Since PEDRI also provides a quantitative measurement, it is possible to track the change in oxygenation kinetics over days.

Fig. 6 shows the enhancement of proton signal by the Overhauser effect in an SCC VII tumor bearing mouse (right hind leg) using two different EPR saturating power levels (75). Electron spin-density images and oxygen images can be obtained from these images. These oxygen images were verified by direct comparison with Eppendorf electrode measurement. The pO_2 images of the tumor (Fig. 6B) show distinct intra-tumor heterogeneity with a gradation of oxygen concentration. The pO_2 values range from hypoxic to normoxic values (~50 mmHg) and are comparable with tumor pO_2 values reported in using different invasive methods. The imaging times ranged between 4 and 8 min, and degradation of pO_2 maps caused by animal motion, system instability, and the contrast agent distribution were not observed during this period. This study also shows that PEDRI is capable of monitoring changes in tumor oxygenation in response to the alteration of the breathing gas. In general, mean pO_2 values increased during Carbogen (95% oxygen and 5% carbon dioxide) breathing (Fig. 6C). In particular, the percentage of extremely hypoxic regions (~5 mmHg pO_2) decreased ~30% during Carbogen breathing. The result explains the previous reports that the treatment efficiency improved when the tumor was oxygenated either by letting the subject breathe Carbogen (41, 50, 75, 92) or when the patient was confined to a hyperbaric oxygen chamber (2, 6, 14, 22). The results from this study showed the capability of PEDRI in obtaining quantitative maps of in vivo tumor oxygen status non-invasively.

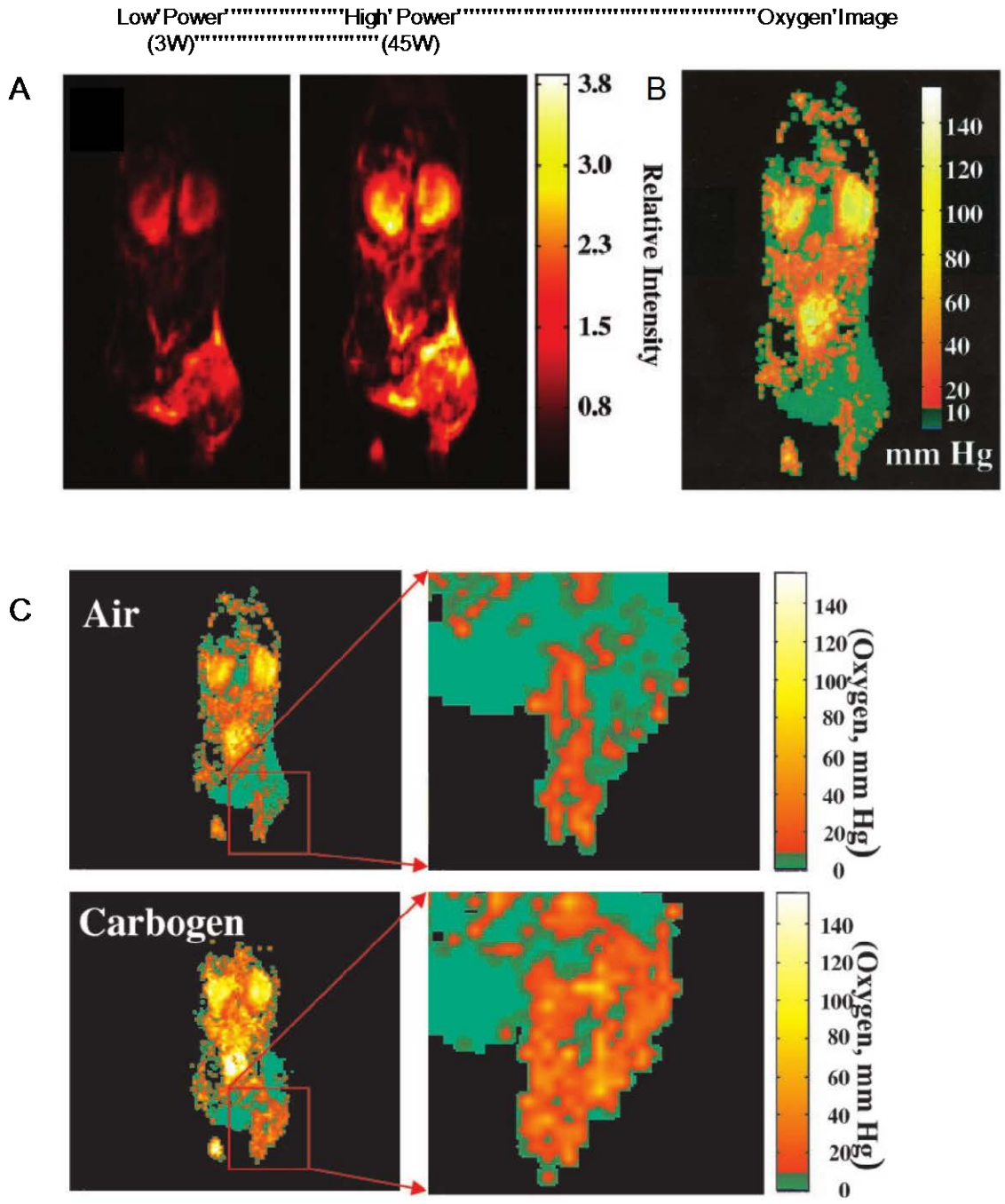

Figure 6

(A), PEDRI with two different EPR irradiation power (right: 3W, left: 45W).**(B)**, calculated pO_2 map based on Fig. 6A. **(C)**, pO_2 images of a C3H mouse with a 1-cm diameter SCC tumor during air breathing (Fig. 6C top) and carbogen breathing (Fig. 6C bottom). The expanded tumor region, given at right, clearly shows heterogeneity in pO_2 distribution. Reprinted by permission from Krishna et al., Proc.Natl.Acad.Sci.USA 99, 2216-21 (2002) (ref. (75)).

Permeability mapping with PEDRI

PEDRI can also be used for simultaneous assessment of tumor pO_2 as well as permeability of the tumor vasculature since the TAM derivative Ox63 is localized to the extracellular, extra vascular space in a similar way to the widely-used Gd^{3+} complexes. In normal tissue, there is a balance between proangiogenic and antiangiogenic factors, where mature vasculature with regular architecture ensures adequate supply of nutrients and oxygen. However, in tumors, because of excess proangiogenic factors (37, 95), tumor neo-vasculature is abnormal and chaotic in architecture and has poor structural integrity (61). The lack of adequate pericyte and endothelial coverage results in large vascular pores causing a marked regional heterogeneity in tumor perfusion and making the tumor vascular hyper-permeable (29, 62). As a result, tumor progression is associated with disorganized angiogenesis, which results in inadequate oxygen supply and limited delivery of chemotherapeutics to the tumor (15, 63). Thus, non-invasive vascular permeability imaging will be useful in evaluating the tumor vasculature and choosing treatment strategy. Leakage of exogenously administered tracers from blood vessels can be used to assess the tumor vascular permeability (91). Especially the most commonly used TAM (Ox63: molecular mass 1427) has a molecular mass three times larger than typical gadolinium complexes, which makes its endothelial transport more sensitive to microvascular permeability. With PEDRI, the tissue microvascular permeability imaging can be acquired using the same datasets that are needed for oximetry. The endothelial transfer coefficient K^{trans} was obtained from pharmacokinetics analysis of the contrast agent-induced dynamic signal change that provides useful data to quantify the treatment response in anticancer therapy.

Fig. 7 shows the comparison of K^{trans} maps of gadolinium-diethylenetriamine pentaacetic acid (Gd-DTPA) and Ox63 with corresponding anatomy image (Fig. 7A) (91). Relatively high K^{trans} values were observed globally for Gd-DTPA (Fig. 7B) compared to those for Ox63 (Fig. 7C) in both tumor and normal tissue regions. The result was consistent with its lower molecular mass making it penetrate easily even through the smaller pores in normal blood vessels (21, 116). Therefore, the K^{trans} of Gd-DTPA may have larger contributions from blood perfusion in tissue than vascular permeability as reported (4, 116). Fig. 7D is a corresponding pO_2 map computed from the same PEDRI images for Ox63 K^{trans} map. The inverse relationship between Ox63 K^{trans} and pO_2 suggested that the leaky and abnormal tumor vasculature is unable to deliver oxygen efficiently to tissue, in agreement with earlier studies using immunohistochemical analyses or oxygen sensitive electrodes (28, 66). This study showed that tumor regions with

high vascular permeability (K^{trans} of Ox63) could be hypoxic regardless of blood perfusion as determined by MRI using Gd-DTPA (K^{trans} of Gd-DTPA), suggesting that diffusion-limited hypoxia does not completely determine the oxygen status of tumors (Fig. 7D and 7F).

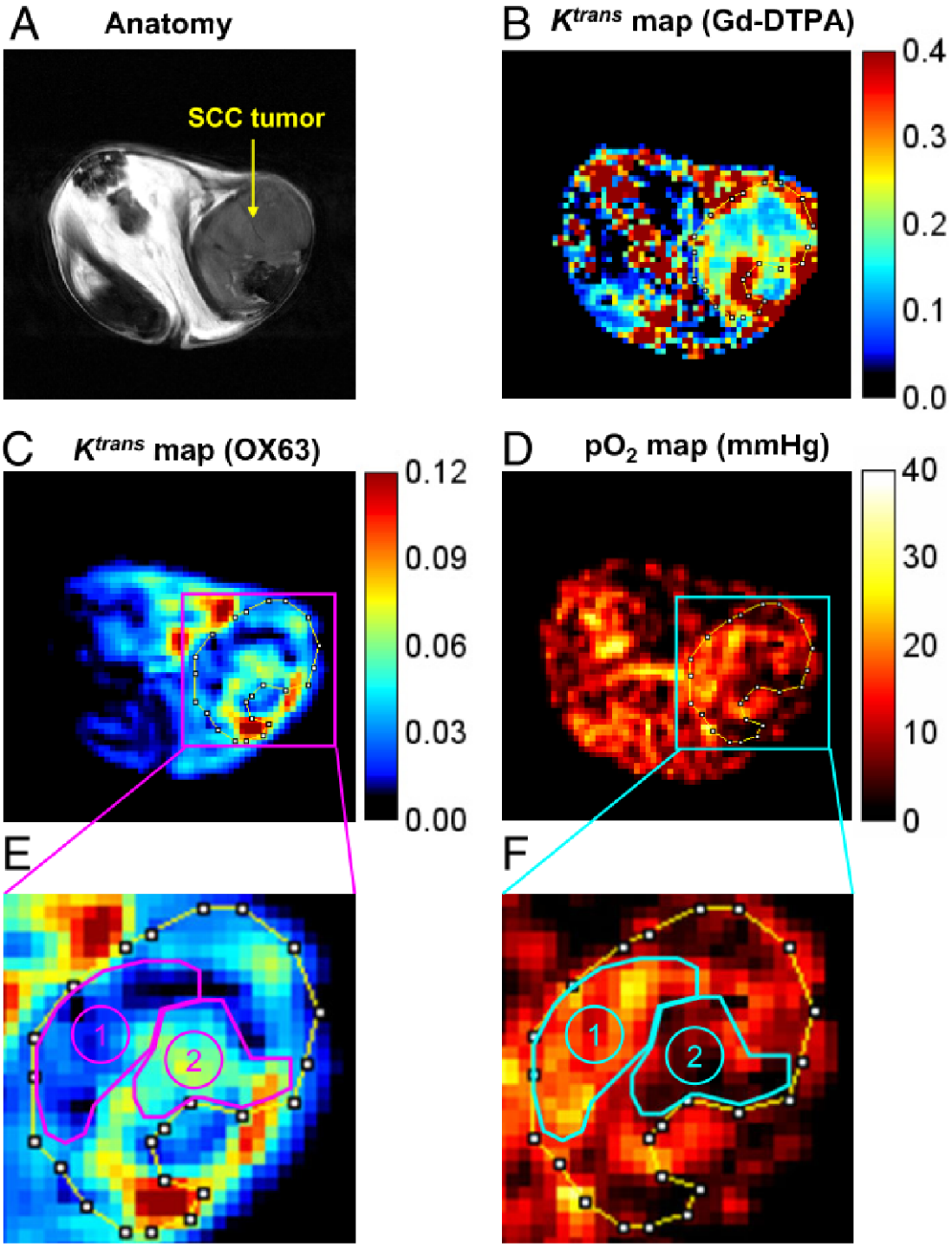

Figure 7

Comparison of K^{trans} maps of Gd-DTPA and Ox63 in a SCC tumor. (**A**), SCC tumor region can be distinguished in a T_2-weighted anatomic image by using 7-T MRI. FOV = 32 mm. (**B**), K^{trans} map of Gd-DTPA using 7-T MRI in SCC tumor-bearing mouse. (**C**), K^{trans} map of Ox63 using PEDRI of the same SCC tumor. Note PEDRI/Ox63 images were obtained before the 7-T MRI/Gd-DTPA study. (**D**), Corresponding pO_2 map computed from the same PEDRI images for K^{trans} Ox63 map. (**E** and **F**), Based on the anatomical image, ROI of SCC tumor was selected and enlarged. Tumor region with low K^{trans} Ox63 values (ROI 1) was relatively oxygenated and normal muscle tissue, and the region with high K^{trans} Ox63 values (ROI 2) coincided with hypoxia in pO_2 image. Reprinted by permission from Matsumoto et al., Proc.Natl.Acad.Sci.USA 99, 2216-21 (2002) (ref. (91)).

Redox mapping with PEDRI

Oxidative stress is associated with various diseases such as cancer, cardiovascular disease, Alzheimer's disease (87), Parkinson's disease (64), diabetes mellitus (86), atherosclerosis (113), ischemia reperfusion injury (18) and chronic inflammatory processes (24). The main causative factors are reactive oxygen species (ROS) which also act as essential cellular messengers and redox regulators (30). Therefore, developing in vivo non-invasive redox imaging can shed light not only on these pathologies but also healthy tissue. Utsumi et al. utilized the PEDRI technique for redox imaging by using redox sensitive nitroxyl radical probes in vitro and in vivo using novel isotope-labeled probes (5, 57, 72, 90, 112, 125, 133). Nitroxyl radicals are known to lose paramagnetic their property via redox reaction with the hydroxyl radical or the superoxide anion radical (Scheme 3) (76, 129). There is a good linear relation between the generation of hydroxyl radical and the loss of paramagnetism of nitroxyl radical (110). It was also reported that cytochrome P-450, NAD(P)H dependent cytochrome P450 oxidoreductase in microsomes is associated with the loss of paramagnetism of nitroxyl radical and reduction of nitroxyl in the mitochondorial electron transport system (58, 59, 103, 123). Glutathione and ascorbic acid are also known to support the reduction of nitroxyl radical (23, 121) and the 2,2,6,6-ethyl substitution of TEMPO (*2,2,6,6*-Tetramethyl-1-piperidinyloxy) led to resistance toward the reduction with ascorbic acid (71). In such manner, the nitroxyl radical directly and indirectly reflects the redox state. Hence, analyzing the in vivo conversion rate of the nitroxyl to the diamagnetic state enables visualization of the redox state. Unlike the chemically-stable TAM for oximetry, nitroxyl radicals used for redox imaging need to participate in redox reactions.

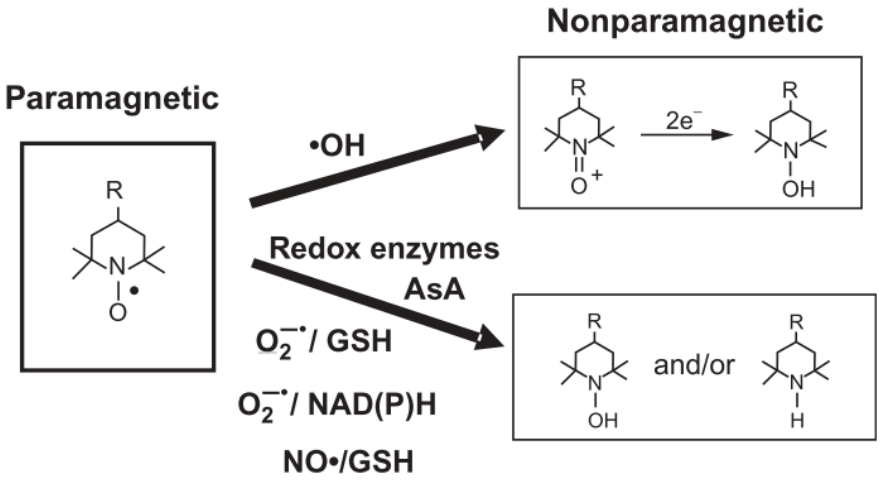

Scheme 3

Reactions that cause loss of nitroxyl radicals. Reprinted by permission from Utsumi and Hyodo, In: Methods in Enzymology, 1st ed. Elsevier Inc., pp 553–571, (2015) (ref.(124)).

To optimize the adaptability of nitroxyl radicals as probes, adequate modifications need to be made. Such chemically modified nitroxyl radicals preferentially distribute in intracellular, extracellular and cell membrane (109). A set of redox-responsive probes to simultaneously assess redox reactions intra- and extracellular regions were reported by Utsumi et al (125). With the design of ^{14}N and ^{15}N labeled nitroxyls, it was possible to distinguish between intra- and extracellular redox processes as demonstrated in a phantom object.

The feasibility of redox imaging using nitroxyl radicals was validated by in vitro experiments (Fig. 8), showing the time-dependent redox reaction of both membrane-permeable $^{14}N/^{15}N$- 3-methoxycarbonyl-2,2,5,5-tetramethyl-pyrrolidine-1-yloxy (MC-PROXYL) and membrane-impermeable $^{14}N/^{15}N$ carboxy-PROXYL. Images were acquired separately by changing the external magnetic field for EPR irradiation between ^{14}N and ^{15}N nuclei in FC-PEDRI (125). Fig. 8A is a schematic of seven phantom tubes comprising six outer tubes with liposomes encapsulated with 100 mM ascorbic acid: two containing the ^{15}N compounds are shown with red, two containing the ^{14}N compounds are shown with blue, two containing both compounds are shown by the red and blue stripes. There was also one central tube, containing both compounds and no liposomes. Carboxy-PROXYL does not penetrate liposome membrane whereas MC-PROXYL can permeate freely across the membrane and undergo 1-electron reduction to the corresponding hydroxylamine. Three such PEDRI images taken at 2.9 min, 13.9 min, and 24.9 min are shown in Fig. 8B. The image

data showed that the intensity from the tubes containing MC-PROXYL in the presence of ascorbic acid-encapsulating liposomes gradually decreased with time, whereas the image intensities from tubes containing carboxy-PROXYL were constant. The rate of intensity loss from each pixel represents the differential redox imaging (Fig. 8C). It should be noted that the rate of intensity loss in the tube containing both MC- and carboxy-PROXYL (indicated with stripes in Fig. 8A) was the same as that in the tube containing either MC- or carboxy-PROXYL. Results from these phantom studies suggested that, if two nitroxyl radicals with different isotopic substitution and different ring substituents (which direct them to different subcellular regions) lose or gain their paramagnetism, then their oxidation and reduction can be spatially resolved and distinguished. The time-dependent signal loss of the PEDRI images was observed when the nitroxyl radicals, which can permeate the liposomal bilayer, underwent reduction, whereas the nitroxyl agent incapable of crossing the membrane bilayer remained intact and signal loss of the PEDRI images was not observed. This capability demonstrated that PEDRI combined with dual-labeled nitroxyl spin probes enabled visualization of events occurring at a nanometer scale, regardless of the intrinsic image resolution of 0.1 mm. This capability further exploited the fact that nitroxyl radicals are efficient antioxidants that also provide protection against oxidative stress in several modalities.

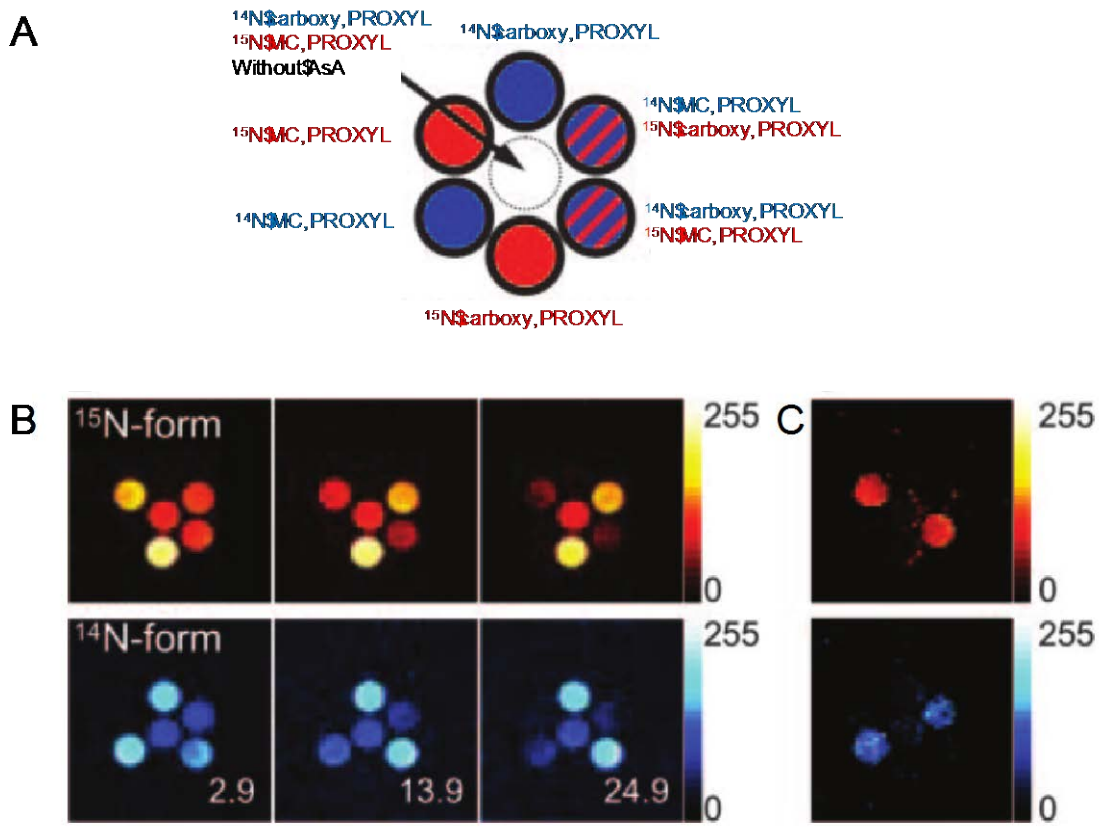

Figure 8

Simultaneous and time-dependent PEDRI of $^{15}N/^{14}N$-carboxy- PROXYL and $^{15}N/^{14}N$-MC-PROXYL in liposomes encapsulating ascorbic acid (100 mM). (**A**), Seven phantom tubes containing ^{14}N-labeled and/or ^{15}N-labeled nitroxyl radicals in the presence and the absence of liposomes were placed in the PEDRI so that images of ^{15}N- and ^{14}N-enhanced images (red and blue, respectively, in Fig. 8B) were obtained simultaneously at the times shown in the figures. (**B**), The presence of ^{15}N-carboxy-PROXYL and ^{15}N-MC-PROXYL are clearly shown by the red color, and ^{14}N-carboxy-PROXYL and ^{14}N-MC-PROXYL by the blue color. (**C**), The images of the decay rates for ^{14}N- and ^{15}N-enhanced PEDRI images were calculated by assuming first- order kinetics for the time-dependent decrease of the contrast (Fig. 8B). Only MC-PROXYL showed decay images in both ^{14}N- and ^{15}N- enhanced PEDRI. (FOV, 48 x 48 mm; matrix, 64 x 64; slice thickness, 10 mm; TR/TE/T^{ESR}, 1,200/25/600 ms. Reprinted by permission from Utsumi et al., Proc.Natl.Acad.Sci.USA 103, 1463-8 (2006) (ref. (125)).

Based on the results from in vitro experiments, in vivo redox imaging using PEDRI was also successfully achieved. Fig. 9 shows in vivo redox imaging demonstrated in bupivacaine (BPVC) induced local inflammation model in mouse legs (36). BPVC is a clinically used local anesthetic agent. However, it is known to destroy skeletal muscle fibers and cause severe inflammation when injected (7, 77, 106). Within several hours of BPVC-induced muscle transient fiber destruction, inflammatory cells locally infiltrate into treated tissues; the muscle cell itself regenerates within several

weeks. Because of this effect, BPVC treatment has been used to create an animal model of muscle inflammation and regeneration. To non-invasively monitor redox status of the muscle, in vivo PEDRI was performed at 4 and 24 h after BPVC treatment in living mice. Two nitroxyl radicals, the cell membrane penetrable (carbamoyl- PROXYL: Fig. 9A) and the cell impermeable (carboxy-PROXYL: Fig. 9B), were used in the in vivo PEDRI experiments to confirm whether the redox reaction mainly occurs in the intracellular or extracellular compartment. Nitroxyl radical solution was carefully injected to the same region of the mouse leg that had received BPVC pretreatment. After injection of carbamoyl-PROXYL, image intensities of both control and BPVC-treated legs (at 4 or 24 h) were clearly enhanced, and this intensity decreased over time. Although the image intensities of both legs were similarly decreased at 4 h after BPVC treatment, the image intensity of the BPVC-treated leg at 24 h showed faster decay than that of the untreated leg. The redox maps clearly illustrated differences in decay rates and distributions between control and BPVC treated legs. The average decay rate observed in the BPVC-treated legs of 8 mice significantly increased at 24 h but not at 4 h. Differences in decay rates of BPVC-treated and contralateral (non-treated) legs in individual mice were also calculated (Fig. 9A, 9B, right panels). In these panels, a symbol above the line marked “even” indicates that the decay rate of the BPVC-treated leg was faster than that of the control leg.

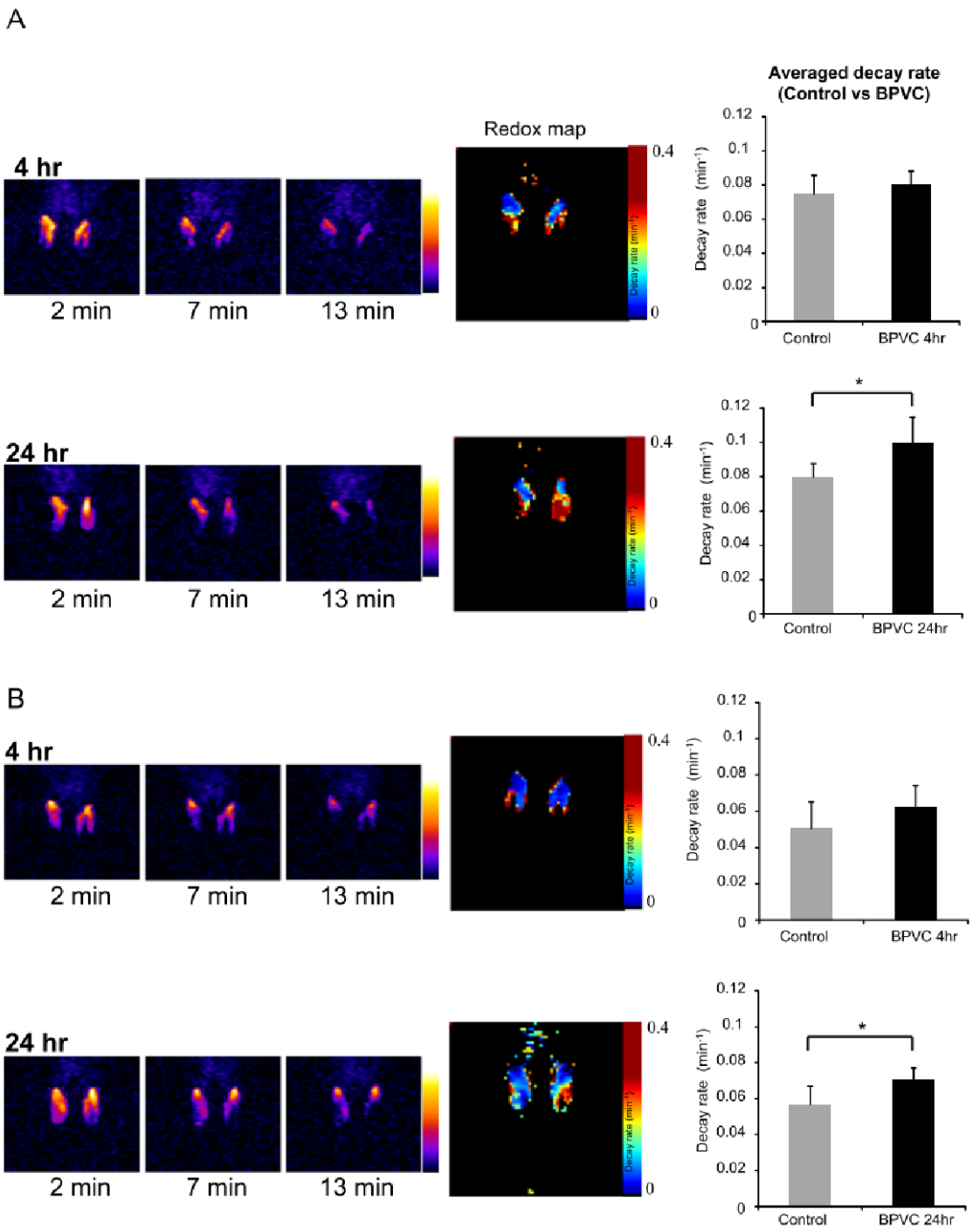

Figure 9

Redox imaging of muscle in BPVC-treated mice using in vivo DNP-MRI. (**A**), In vivo DNP-MRI images and redox maps at 4 and 24 h after BPVC treatment in mice. Images were taken after injection of 2.5mM carbamoyl-PROXYL (50 µL) into both legs. Redox maps were calculated using four pharmacokinetic in vivo DNP-MRI images. Decay rates were calculated for the DNP-MRI images of untreated and BPVC-treated legs. Plots showing differences between decay rates in BPVC treated vs untreated (contralateral) legs in individual mice. (**B**), in vivo DNP-MRI images and

redox map at 4 and 24 h after BPVC treatment in mice. Images were taken after injection of 2.5mM carboxy-PROXYL (50 μL) into both legs. (N = 8 per group). * $p < 0.01$. (Other parameters are plotted as for carbamoyl-PROXYL.). Reprinted with permission from Eto et al., Free Radic.Biol.Med. 89, 1097-1104 (2015) (ref. (36)).

It has been reported that probes that have multiple hyperfine lines can have efficient Overhauser enhancement. When the MRI signal enhancement by saturating electron of such probes is enough to visualize in vivo free radicals, several endogenous antioxidants can be used as redox responsive PEDRI probes. In contrast to administering the redox sensitive nitroxyl probe and observing the loss of signal, the attempt to visualize and identify various endogenous free radical intermediates derived from redox transformations was tested (56, 124).

Fig. 10 shows the EPR signals of the intermediate of various candidate probes (56). The enhancements due to FADH and FMNH were similar to that induced by carbamoyl- PROXYL (enhancement factor = 3.8, 4.3 and 3.3, respectively), even though the EPR absorption spectra of both FMNH and FADH exhibit 13-fold broader line width, compared with the spectrum of carbamoyl-PROXYL, and the ratios of enhancement factor to peak height of both FMNH and FADH were 4−7 times higher than that of carbamoyl-PROXYL. The line widths varied from 4.2 MHz (carbamoyl-PROXYL) to 58.5 MHz (FMN), which were much larger than the MRI resonance frequency. EPR excitation for PEDRI was carried out under continuous-wave irradiation, and the fluctuation of EPR irradiation was estimated within 1 ppm (corresponding to 0.5 kHz), which probes only a small proportion of the free radical molecules. This allows the electron transitions to be saturated much less completely in FMNH and FADH solutions than in carbamoyl-PROXYL solution. The $CoQ_{10}H$ and radicals of vitamins E and K all enhanced the proton signals of the non-aqueous solvent: acetone for $CoQ_{10}H$, hexane for the vitamin E radical, and $CHCl_3$ / EtOH for the vitamin K radical. Compared with carbamoyl-PROXYL, the ratio of enhancement factor to peak height was 38 times higher for the vitamin K_1 radical, 5 times higher for the vitamin E radical, and 2 times higher for $CoQ_{10}H$. Also, the electrons of these probes can be separately saturated and induce DNP by adjusting the EPR irradiation frequency. The result indicates that it possible to simultaneously visualize various free radical intermediates of endogenous redox molecules (56).

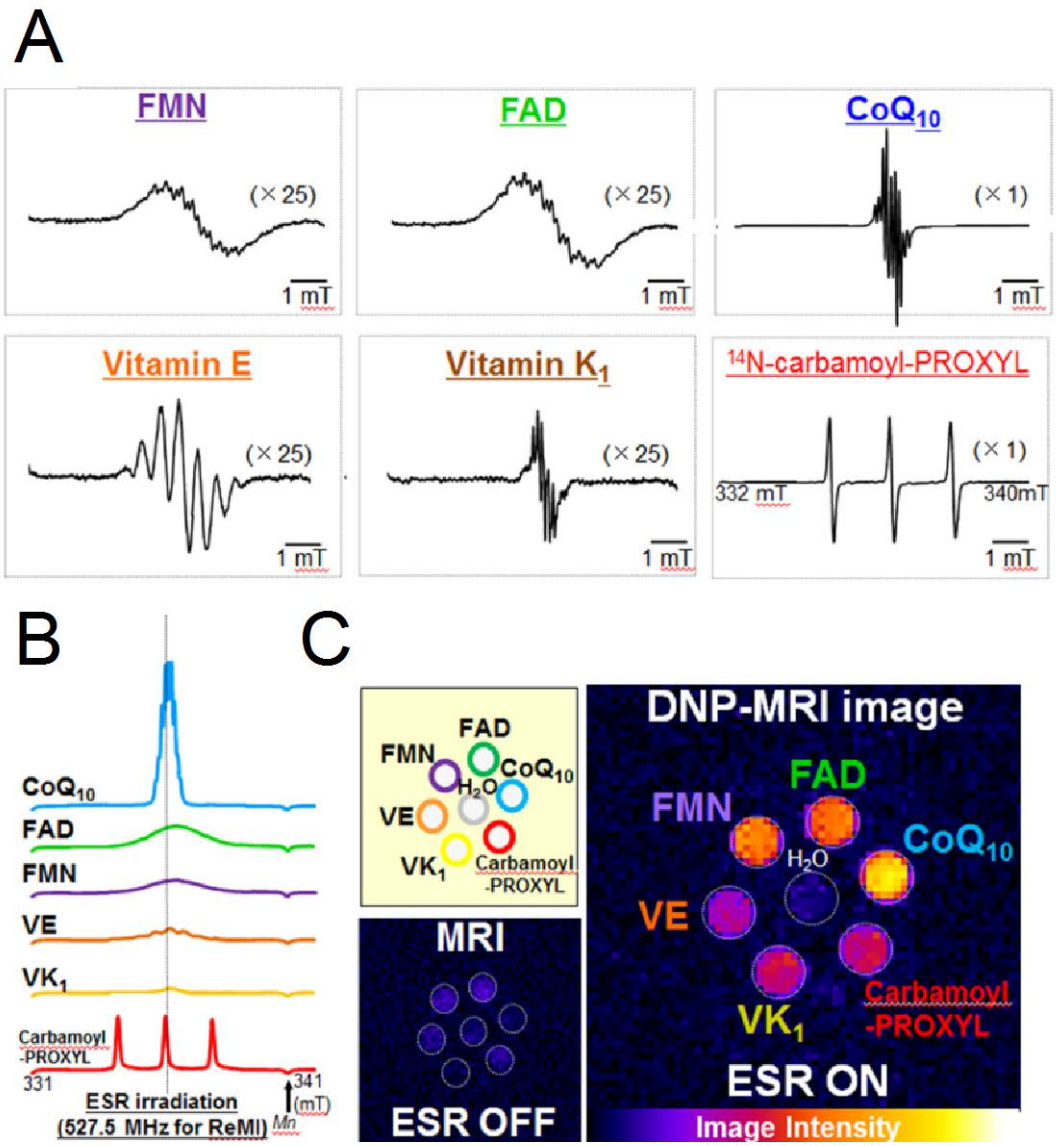

Figure 10

Typical EPR spectra (**A**), the absorption EPR spectra (**B**), and simultaneous DNP-MRI image (**C**) of free radical intermediates from FMN, FAD, CoQ_{10}, vitamin E, vitamin K_1, and the synthetic stable radical 14N-carbamoyl-PROXYL. The vertical solid line in part b indicates the frequency of EPR irradiation for PEDRI (527.5 MHz), which is the resonance frequency of the central peak of carbamoyl-PROXYL. MRI spectra with and without EPR irradiation were obtained with a spin echo sequence at 850 kHz using a homemade in vivo PEDRI system kept at room temperature. Adapted from with permission. Reprinted (adapted) with permission from Hyodo et al., Anal.Chem. 86, 7234-7238 (2014) (ref. (56)). © 2014 American Chemical Society.

pH Mapping with PEDRI

Aberration of normal tissue pH homeostasis in the human body has been reported for a number of pathological conditions that include cancers (124, 135), myocardial (98) and brain ischemia (73, 132), chronic pulmonary (60) and kidney diseases (74). The extracellular tumor tissue acidosis, pH_e, has been identified as a significant factor in cancer pathophysiology contributing to tumor initiation, progression, and therapy (43). Therefore, *in vivo* pH_e imaging of tumor tissue microenvironment (TME) may provide an invaluable tool for diagnosis, understanding of disease progression and treatment optimization. Recently-developed Variable Field (VF) (69) and Variable Radio Frequency (VRF) PEDRI (32) approaches allow for functional mapping using nitroxide or trityl probes while additionally keeping the capability to provide anatomical images. VF(69) and VRF PEDRI (32) approaches allow for mapping chemical microenvironment using probes with functionally-dependent ratiometric spectral parameters. The valuable spectral parameters at each pixel can be extracted from a limited number of PEDRI acquisitions acquired at pre-selected EPR excitation fields or EPR excitation frequencies. This allows for functional mapping using specifically-designed paramagnetic probes, together with high quality spatial resolution and short acquisition time. The concept was first verified using VF PEDRI and a pH sensitive nitroxide probe (69).

Fig. 11 shows typical DNP spectra of the nitroxide NR1 acquired in acid, pH 4.98, and slightly alkaline, pH 7.62, aqueous solutions corresponding to dominant contributions of the protonated, RH^+, and nonprotonated, R, forms of the radical, correspondingly, pK_a=6.1 (70). The significantly larger distance between the outer lines of the triplet spectra observed for the alkaline solution of the nitroxide is in agreement with previously reported larger nitrogen hyperfine splitting for the R form (70).

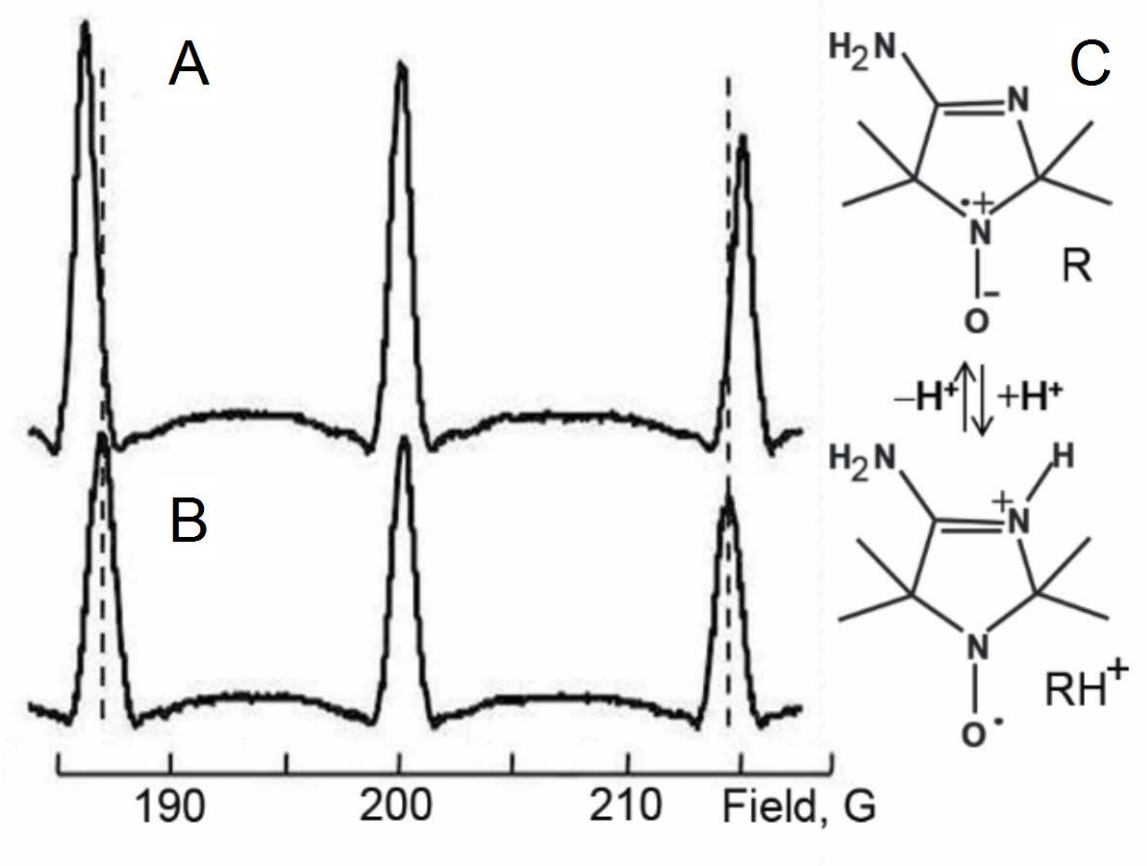

Figure 11

FC-DNP spectra of the nitroxide NR1 obtained in phosphate–citrate buffer (10 mM each) at pH 7.62 (**A**) and pH 4.98 (**B**), and the scheme of the reversible protonation of the NR1 radical, pK_a=6.1 (**C**). Frequency of EPR irradiation 563.2 MHz, irradiation time, 500 ms, repetition time, 1140 ms; step size = 0.04 G; P =0.8 W, sample volume, 5 ml. The preferable resonance structures of protonated, RH^+, and unprotonated, R, forms are shown illustrating higher unpaired electron density on nitrogen atom N-1 in the unprotonated form. Protonation results in a DNP-detected difference in hyperfine splitting (Δa_N=0.8 G) between R and RH^+ forms. A dotted line is extended from low- and high-field peaks of the spectra (B) to aid the eye. Reprinted by permission from Khramtsov et al., J.Magn.Reson. 202, 267-73 (2010) (ref.(69)).

The chemical equilibrium shown in Fig. 11 illustrates the effect of protonation of the atom N-3 of the radical heterocycle resulting in decreasing unpaired electron density at the nitrogen nucleus of the N-O fragment, and, as a consequence, in lowered hyperfine splitting (hfs) for the RH^+ form. Note that at low EPR frequency, 563.2 MHz in Fig. 12, the three lines of the spectrum are unequally spaced due to the Breit–Rabi effect (13, 102).

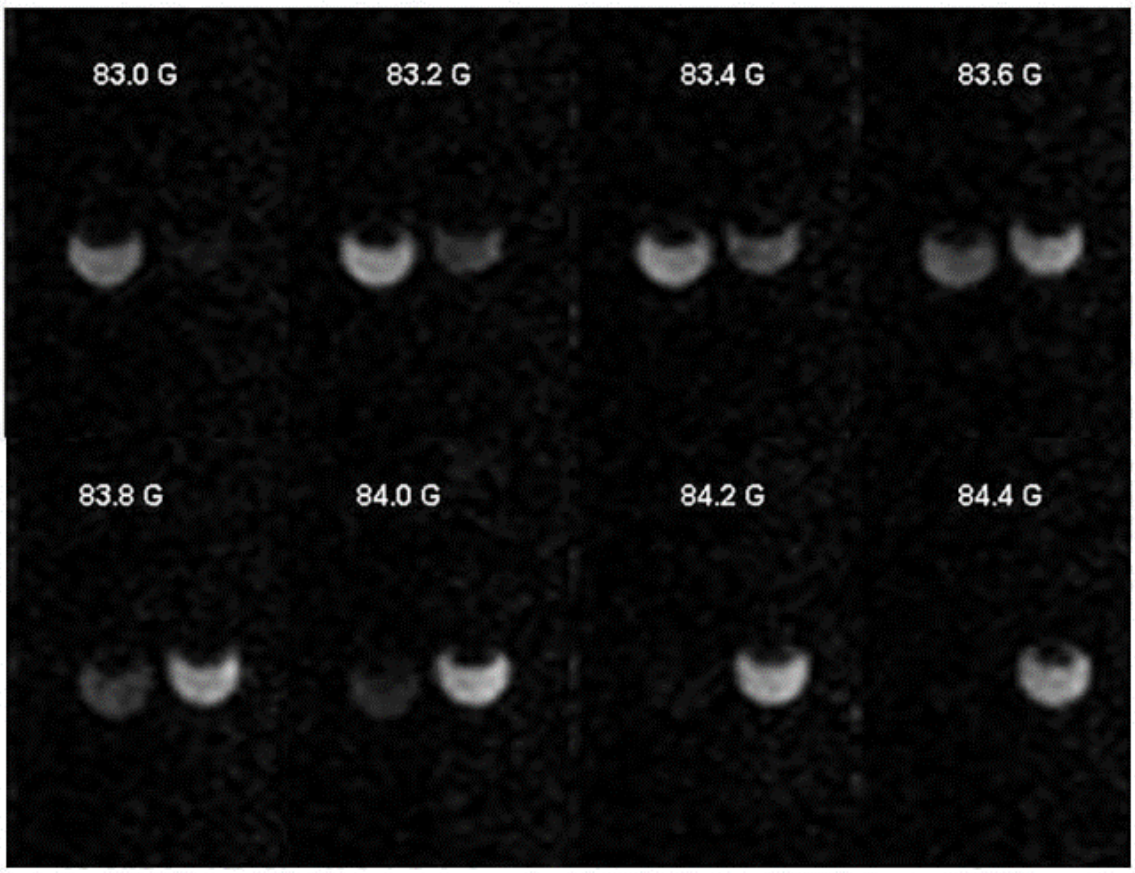

Figure 12

Sequence of PEDRI images of the phantom sample of a pair of tubes, 10 mm diameter, containing 1 mM aqueous solutions of the NR1 probe at pH 9 (left tube) and pH 2 (right tube). Images were acquired at EPR frequency 282 MHz (100 G for the EPR center field) with evolution field stepped in the range from 83.0 G to 84.4 G around the position of the low-field EPR component of the NR1 triplet spectrum. The observed variation of the image intensity with the shift in EPR irradiation field, B^{EPR}, illustrates the subsequent changes with the maximal image intensity of R form (left tube) and RH^+ form (right tube) when B^{EPR} is equal to 83.2 G and 84 G, respectively. Reprinted by permission from Khramtsov et al., J.Magn.Reson. 202, 267-73 (2010) (ref.(69)).

The pH-dependent DNP spectral changes allow for preferable excitation of EPR resonances of R or RH^+ forms of the nitroxide NR1 as illustrated in Fig. 12 for the phantom sample of the two tubes filled with an aqueous solution of NR1 titrated to alkaline and acidic pH values. The stepped variation of the EPR irradiation field, B^{EPR}, resulted in the subsequent changes in image intensity with the maximal image intensities of alkaline (predominantly R form) and acidic (predominantly RH^+ form) solutions when B^{EPR} is equal to 83.2 G and 84 G, respectively. Note that the observed 0.8 G difference in B^{EPR} values between the brightest images of R and RH^+ forms is in excellent agreement with maximal pH dependent change of hfs shown in Fig. 11.

Based on the data shown in Fig. 12, EPR excitation at the field values that coincide with DNP spectral peak positions of RH^+ and R forms of the probe will generate two PEDRI images with signal intensities proportional to the concentrations of the corresponding ionization states of the probe. Taking into account that the ratio of concentrations of protonated and nonprotonated forms of the probe is directly related to pH ($[RH^+]/R)=[H^+]/K_a$), this provides an opportunity to convert these two PEDRI images into a pH map.

Alternatively to VF PEDRI, the VRF PEDRI approach uses a stationary magnetic field but different EPR RF frequencies. The ratio of Overhauser enhancements measured at each pixel at two different excitation frequencies corresponding to the resonances of protonated and deprotonated forms of a pH-sensitive nitroxide is converted to a pH map using a corresponding calibration curve. Elimination of field cycling decreased the acquisition time by exclusion of the periods of ramping and stabilization of the magnetic field. Improved magnetic field homogeneity and stability allowed for the fast MRI acquisition modalities such as fast spin echo. In total, about a 30-fold decrease in EPR irradiation time was achieved for VRF PEDRI (2.4 s) (69) compared with VF PEDRI (70 s) (32) as tested with similar aqueous solutions of the NR1 radical. This is particularly important for in vivo applications enabling one to overcome the limiting stability of paramagnetic probes and sample overheating by reducing RF power deposition.

To perform PEDRI pH_e mapping of TME there is a need for paramagnetic pH probes that meet the following requirements: (i) appropriate pK_a values in the range from 6.1 to 6.9 that allow pH measurements of slightly acidic TME pH values; (ii) comparatively narrow linewidth to obtain a high enhancement and decrease RF power deposition; (iii) sufficient stability of paramagnetic fragments in highly reducing tumor microenvironment, and (iv) hydrophilic structure that ensures extracellular probe localization. The nitroxide NR1 used to prove the concept of VF and VRF PEDRI (32, 69) has a very short life-time in vivo due to its fast reduction to the corresponding hydroxylamine and its applications *in vivo* are hardly possible.

The nitroxide NR2 represents the structure (see Scheme 4a) of a paramagnetic pH probe carefully designed for in vivo monitoring of pH_e in TME. The pK_a value of the probe has been tuned by variation of substitute at position 4 of radical heterocycle resulting in optimal range of pH sensitivity centered at slightly acidic pH_e of TME (pK_a=6.6 at 37 ^oC). Partial deuteration of the NR2 resulted in the narrowing EPR line (1.2 G for NR2 vs. 2.1 G for undeuterated analog) required for efficient saturation by RF irradiation which is of critical importance for obtaining higher PEDRI enhancement and allowing for shorter acquisition time. The bulky ethyl substitutes at positions 2 and 5 of the radical heterocycle of the NR2 serve to protect the paramagnetic NO fragment against bioreduction, significantly enhancing

its biostability. Extracellular localization of the probe has been achieved by binding the nitroxide label to hydrophilic tripeptide, glutathione, preventing the resulting NR2 probe from diffusion across the hydrophobic lipid bilayer of the biomembranes and therefore, enforcing probe localization in extracellular aqueous volumes (108).

Fig. 15A-D shows the pH calibration of the NR2 probe using VRF PEDRI obtained for a 10-tube phantom (Fig.15a) containing the NR2 solutions of different pH values. EPR frequencies were pre-selected to correspond to the maximal NMR intensities of R and RH^+ forms. A fast spin echo sequence has been applied with an acquisition time of 8.4 s for each image (Fig.15B and 15C). The EPR *off* image was subtracted from both EPR *on* images acquired at RF_1 and RF_2, yielding image intensities, $I(RF_1)$ and $I(RF_2)$, respectively. The pH dependence of intensities ratio $I(RF_1)/(I(RF_1)+I(RF_2))$ shown in Fig. 3d is described by the titration curve with the observed pK_a value of NR2 probe equal to 6.75 ± 0.05 in agreement with the EPR-measured pK_a value, 6.74 ± 0.05 (108).

Fig. 13E-F demonstrates application of VRF PEDRI for pH_e mapping of living tissue in tumor-bearing mouse using the NR2 radical. Two PEDRI images are acquired during 8.4 s EPR irradiation at two pre-selected EPR frequencies which correspond to EPR resonances of RH^+ and R forms of deuterated NR2 probe. The ratio of the signal intensities of these two images correspond to the $[RH^+]/[R]$ ratio, therefore allowing the conversion of two PEDRI images into a pH map using the calibration curve shown in Fig. 15D. The probe distribution area in tumor (Fig. 13E left) is about 1 cm^2 which is close to the value of the tumor cross-sectional area (the measured tumor size is about 1.2 cm×0.9 cm), therefore supporting probe localization within the tumor. The probe distribution area in the mammary gland (Fig. 13E right) is less than 0.2 cm^2 being close to its size. Fig. 13F shows a pH map (in color) superimposed with low-field MRI (gray scale) representing the coronal view of the mouse. The broader pH_e distribution in tumor in the range from 6.4 to 7.1 compared with pH_e distribution in mammary gland from pH 7.0 to 7.2 was observed in agreement with high heterogeneity of the tumor microenvironment. Average values of pH_e in tumor and mammary gland were found to be 6.8±0.1 and 7.1±0.1, respectively, supporting significant tumor tissue acidosis. Note that sufficiently long reduction rate of the NR2 even in highly reducing tumor tissue ($\tau_{1/2} \approx 5$ min) allowed for quantitative assessment of spatially-resolved information on tissue reducing capacity in complement to pH measurements (11) by mapping decay of PEDRI signal at each pixel. Therefore, the same pH probe can be used for simultaneous mapping of pH and redox status.

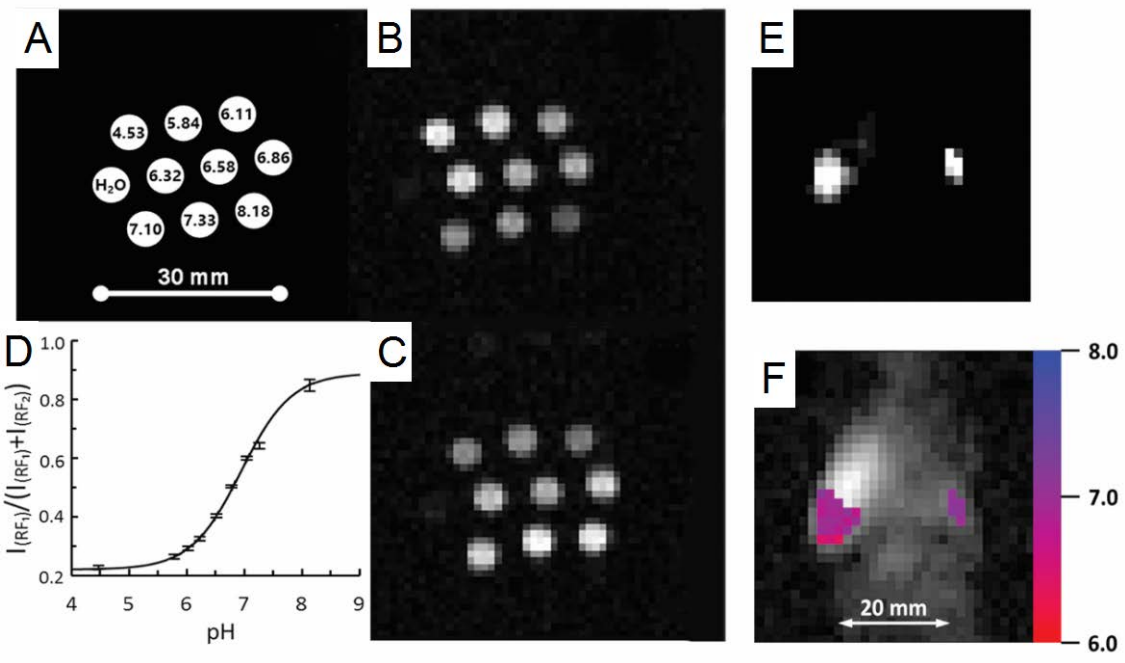

Fig.13.

VRF PEDRI pH calibration (**A-D**) and *in vivo* pH mapping (**E-F**) using NR2 probe. Calibration has been performed using 10-tube phantom (**A**) at room temperature. PEDRI images were acquired at two EPR irradiations, RF_2=559.3 MHz (**B**) and RF_1=562.1 MHz (**C**), acquisition time, 8.4 s. The tube with water alone is not visible on either image due to lower intensity compared to signal from tubes containing paramagnetic probe. EPR *off* image (not shown) was subtracted from both EPR *on* images acquired at RF_1 and RF_2, yielding image intensities, $I(RF_1)$ and $I(RF_2)$. (**D**) pH dependence of the ratio $I(RF_1)/(I(RF_1)+I(RF_2))$. Solid line is nonlinear least-squares fit of the data to a conventional titration equation yielding pK_a value equal to 6.75± 0.05. Error bars represent the standard deviation. In vivo PEDRI pH mapping was performed in the anesthetized breast tumor-bearing mouse (**E-F**). Paramagnetic NR2 probe was injected into the tumor (number 4 mammary gland, left) and normal mammary gland (number 9, right). (**E**) Qualitative visualization of the distribution of the NR2 probe, in vivo. The image is the average of two PEDRI images acquired at two EPR frequencies, RF1=562.1 MHz and RF2=559.3 MHz, NMR frequency, 784.9 kHz, matrix, 64 x 64; field of view, 80 x 80 mm. Irradiation time was 8.4 sec for each acquisition. (**F**) pH map (in color) calculated from two PEDRI images superimposed with the MRI image (grey scale) showing the coronal view of the mouse. Reprinted (adapted) with permission from Samouilov et al., Anal.Chem. 86, 1045-52 (2014) ref.(108)). © 2014 American Chemical Society.

Trityl radicals have advantages over nitroxides for in vivo PEDRI applications due to extraordinary high stability in living tissues and long relaxation times allowing for a maximum saturation with limited RF power deposition. These compounds were first developed for biomedical applications by Nycomed Innovation (119) and have been used for in vivo EPR (34) and PEDRI oximetry (75). In addition, trityl derivatives containing amino (27) or phosphono groups (26) demonstrate dual function oxygen and pH spectral sensitivity. Recently trityl probe with spectral sensitivity to

p**H**, *p***O**$_2$ and **P**i (inorganic phosphate) in ***E***xtracellular tissue microenvironment (termed HOP*E* probe, see Scheme 4b) has been synthesized (12, 26) and used for concurrent multifunctional assessment of TME in tumor-bearing mice using low-field EPR spectroscopy (10). To our opinion PEDRI approach in combination with HOP*E* probe provides opportunity for multifunctional mapping of tissue microenvironment in living subjects.

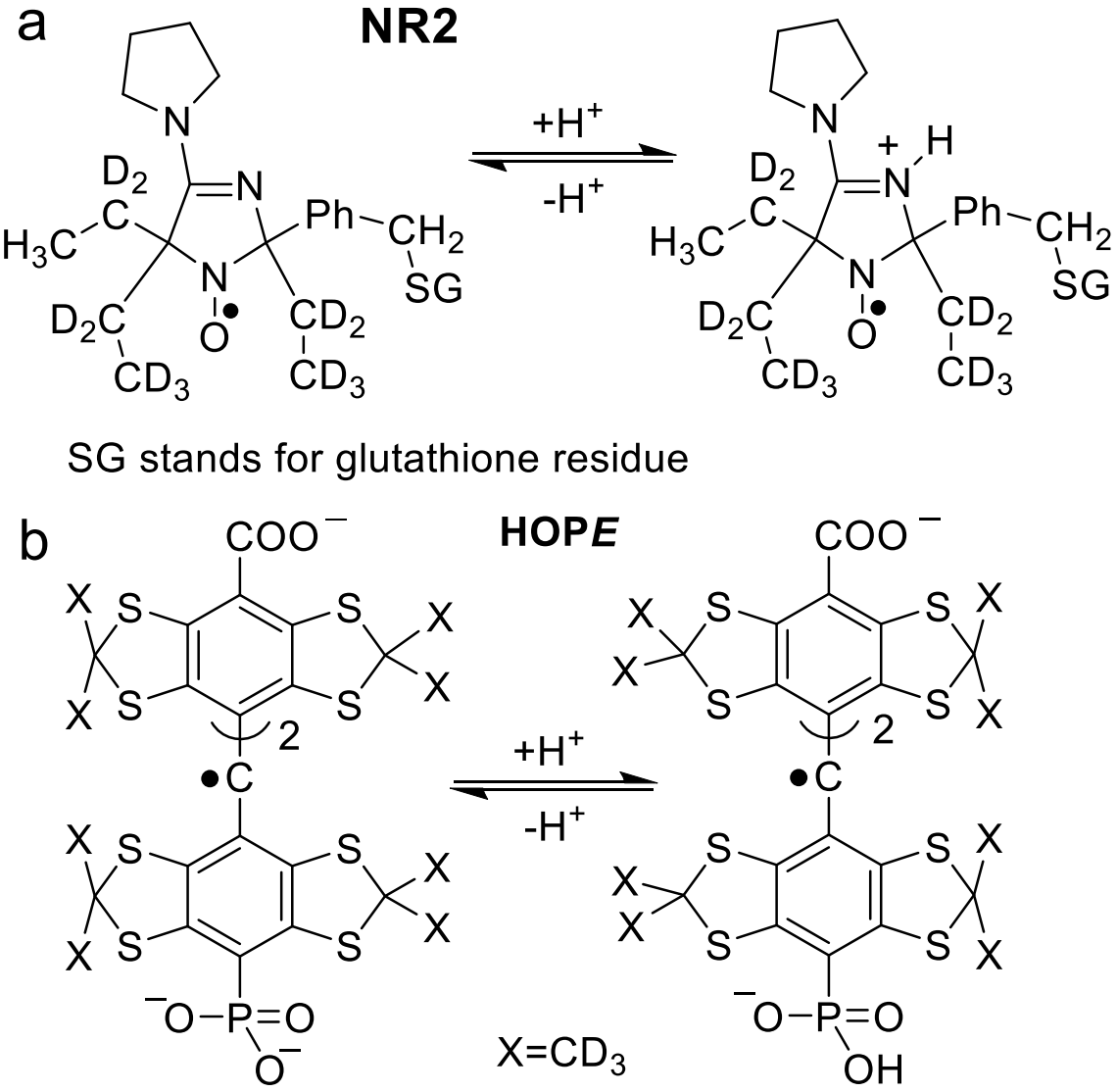

Scheme 4. The chemical structures and proton exchange equilibrium for pH sensitive nitroxide, NR2, and trityl, HOP*E*, probes.

Fig. 14A-D shows VRF PEDRI pH calibration performed using a phantom sample containing anoxic solutions of the HOP*E* probe at different pH values. Acquisitions of two PEDRI images obtained with EPR irradiations at two pre-

selected EPR frequencies that correspond maximal NMR intensities of R and RH^+ forms of the HOP*E* probe (see Scheme 4) allows one to calculate the pH calibration curve shown in Fig. 14D (cf. with Fig. 15A-D for the NR2)(122). In case of dual pH and oxygen mapping the number of acquisition has to be extended by addition of PEDRI images acquired at different RF powers to assess oxygen concentration (75). Fig. 14E-F illustrates dual-function pH and pO_2 mapping of a phantom consisting of four tubes prepared with different pH and oxygen concentrations and obtained by acquisition of a total of four PEDRI images at different EPR frequencies (x2) and different RF powers (x2). The conversion of these images to pH (Fig. 14E) and oxygen (Fig.14F) maps with spatial resolution of 0.6 mm and field of view 40x40 mm^2, provides functional accuracy of about 0.05 pH units of pH and 3-4 mmHg of pO_2 for the physiologically relevant pH and oxygen ranges. The calculated mean values of pH and pO_2 are in reasonable agreement with the experimental ones. Note that acquisition of additional PEDRI images at intermediate EPR frequency, (RF1+RF2)/2, may provide information on the spatial distribution of phosphate due to the fact that Pi facilitates proton exchange between R and RH^+ forms of the HOP*E* probe, therefore resulting in appearance of EPR signal intensity at the intermediate EPR frequency (see review (68) for details).

In summary, VF and VRF PEDRI techniques in combination with functional paramagnetic probes offer opportunity for mapping of specific parameters of local chemical microenvironment, including measurements in vivo. Application of multifunctional radicals such as HOP*E* probes can further extend the capability of PEDRI for concurrent mapping of several chemical parameters of local microenvironment.

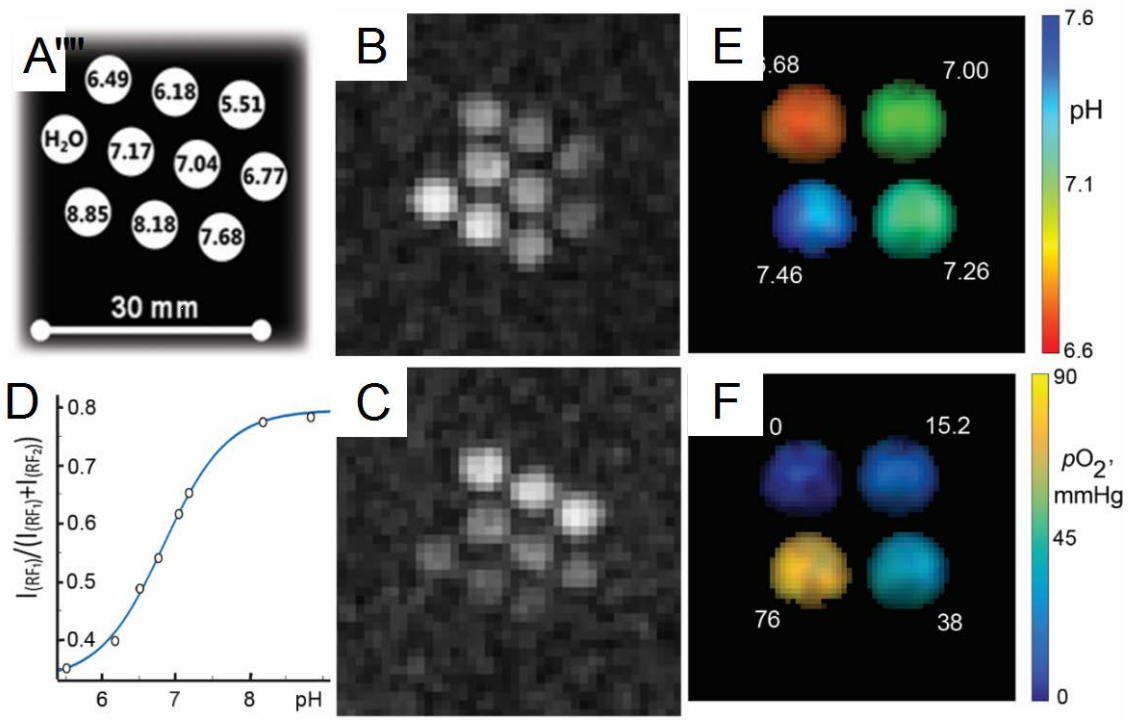

Figure 14

VRF PEDRI pH calibration (**A-D**) and dual function pH and pO_2 mapping (**E-F**) using trityl HOP*E* probe. The phantom used for pH calibration consists of 9 sealed glass tubes filled with 1 ml of degassed 0.5 mM probe solutions, 150 mM sodium chloride, at different pH values indicated in the Figure 14A, and one reference tube filled with degassed solution of sodium chloride only. Images were acquired using RF1=573.625 MHz (**B**) and RF2=573.95 MHz (**C**) EPR irradiation frequencies, respectively; NMR frequency, 856 kHz, irradiation time, 130 s; matrix, 64 x 64; field of view, 80 mm x 80 mm. (**D**) pH dependence of the ratio I(RF1)/(I(RF1)+I(RF2)). Solid line is nonlinear least-squares fit of the data to a conventional titration equation yielding pK_a value equal to 6.9± 0.03. (**E-F**) PEDRI mapping of pH and pO_2 of a phantom sample. The sample consisted of four tubes filled with 1 mM solution of HOP*E* probe of different oxygen concentrations and pH values (indicated in the figures 5e and 5f, respectively). PEDRI images were acquired at two frequencies of EPR radiation, 456.6 MHz and 457 MHz, and at two power values, 0.5 W and 4.0 W. The calculated pH values are 6.72±0.05, 7.04±0.05, 7.27±0.05 and 7.45±0.07, and pO_2 values are 5±3 mmHg, 14±3 mmHg, 35±4 mmHg, and 81±6 mmHg. MRI data was acquired by fast spin echo method, matrix size, 64×64; field of view, 40mm×40 mm, NMR frequency, 686.3 kHz; total acquisition time, 4.2 min. Figures 16A-D reprinted by permission from Takashi et al., Appl.Magn.Reson. 45, 817-826 (2014) (ref.(122)). Figures 16E-F are provided through the courtesy of Artem Gorodetskii, IMMR center, WVU.

Conclusion

PEDRI has been developed since the 1980s as a free radical imaging method based on the Overhauser effect. It has proved to be applicable to in vivo imaging by introducing optimal tracers and pulse sequences. The possibility of generating high resolution PEDRI images with corresponding anatomical images has realized the quantitative

measurement of pO_2, tissue permeability, redox-status and pH. Such functional information obtained from PEDRI has been applied to various disease models preclinically giving insights into the pathology and etiology of human disease.

List of abbreviations

BPVC	Bupivacaine
CoQ10	Coenzyme Q10
DNP	Dynamic Nuclear Polarization
EPR	Electron Paramagnetic Resonance
EPRI	Electron Paramagnetic Resonance Imaging
FAD	Flavin Adenine Dinucleotide
FC	Field Cycling
FMN	Flavin Mononucleotide
Gd-DTPA	Gadolinium-DiethyleneTriamine Pentaacetic Acid
hfs	hyperfine splitting
HOPE	trityl probe with spectral sensitivity to pH, pO_2 and Pi (inorganic phosphate) in Extracellular tissue microenvironment
MC-PROXYL	3-MethoxyCarbonyl-2,2,5,5-Tetramethyl-pyrrolidine-1-yloxy
MRI	Magnetic Resonance Imaging
NMR	Nuclear Magnetic Resonance
NOE	Nuclear Overhauser Effect
OMRI	Overhauser-enhanced Magnetic Resonance Imaging
PCA	Proxyl Carboxylic Acid
PEDRI	Proton-Electron Double-Resonance Imaging
pO_2	Partial pressure of oxygen
RF	Radio-Frequency
ROI	Region Of Interest
ROS	Reactive Oxygen Species
SAR	Specific Absorption Rate
SNR	Signal-to-Noise Ratio
TAM	Triarylmethyl or trityl radical
TEMPO	2,2,6,6-Tetramethyl-1-piperidinyloxy
TEMPOL	4-Hydroxy-2,2,6,6-tetramethylpiperidine-1-oxyl
T^{EPR}	EPR irradiation time
TME	Tumor tissue microenvironment
TR	Repetition Time
VF	Variable Field
VRF	Variable Radio Frequency

References

1 Ahmad R, Kuppusamy P: Theory, Instrumentation, and Applications of Electron Paramagnetic Resonance Oximetry. *Chem Rev* 110: 3212–3236, 2010.

2 Al-Waili NS, Butler GJ, Beale J, Hamilton RW, Lee BY, Lucas P: Hyperbaric oxygen and malignancies: a potential role in radiotherapy, chemotherapy, tumor surgery and phototherapy. *Med Sci Monit* 11: RA279-289, 2005.

3 Andrew ER: N.m.r. Imaging of Intact Biological Systems. *Philos Trans R Soc Lond B Biol Sci* 289: 471–481, 1980.

4 Ardenkjær-Larsen JH, Laursen I, Leunbach I, Ehnholm G, Wistrand L-G, Petersson JS, Golman K: EPR and DNP Properties of Certain Novel Single Electron Contrast Agents Intended for Oximetric Imaging. *J Magn Reson* 133: 1–12, 1998.

5 Benial AMF, Utsumi H, Ichikawa K, Murugesan R, Yamada K, Kinoshita Y, Naganuma T, Kato M: Dynamic nuclear polarization studies of redox-sensitive nitroxyl spin probes in liposomal solution. *J Magn Reson* 204: 131–138, 2010.

6 Bennett MH, Feldmeier J, Smee R, Milross C: Hyperbaric oxygenation for tumour sensitisation to radiotherapy. *Cochrane database Syst Rev*: CD005007, 2012.

7 Benoit PW, Belt WD: Destruction and regeneration of skeletal muscle after treatment with a local anaesthetic, bupivacaine (Marcaine). *J Anat* 107: 547–56, 1970.

8 Berliner J, Fujii H: Magnetic resonance imaging of biological specimens by electron paramagnetic resonance of nitroxide spin labels. *Science (80-)* 227: 517–519, 1985.

9 Berliner LJ, Fujii H: EPR imaging of diffusional processes in biologically relevant polymers. *J Magn Reson* 69: 68–72, 1986.

10 Bobko AA, Eubank TD, Driesschaert B, Dhimitruka I, Evans J, Mohammad R, Tchekneva EE, Dikov MM, Khramtsov V V.: Interstitial Inorganic Phosphate as a Tumor Microenvironment Marker for Tumor Progression. *Sci Rep* 7: 41233, 2017.

11 Bobko AA, Eubank TD, Voorhees JL, Efimova O V., Kirilyuk IA, Petryakov S, Trofimiov DG, Marsh CB, Zweier JL, Grigor'ev IA, Samouilov A, Khramtsov V V.: In vivo monitoring of pH, redox status, and glutathione using L-band EPR for assessment of therapeutic effectiveness in solid tumors. *Magn Reson Med*

67: 1827–1836, 2012.

12 Bobko AA, Dhimitruka I, Zweier JL, Khramtsov V V: Fourier Transform EPR Spectroscopy of Trityl Radicals for Multifunctional Assessment of Chemical Microenvironment. *Angew Chemie Int Ed* 53: 2735–2738, 2014.

13 Breit G, Rabi II: Measurement of Nuclear Spin. *Phys Rev* 38: 2082–2083, 1931.

14 Brizel DM, Hage WD, Dodge RK, Munley MT, Piantadosi CA, Dewhirst MW: Hyperbaric Oxygen Improves Tumor Radiation Response Significantly More Than Carbogen/Nicotinamide. *Radiat Res* 147: 715, 1997.

15 Brown JM, Giaccia AJ: The unique physiology of solid tumors: opportunities (and problems) for cancer therapy. *Cancer Res* 58: 1408–1416, 1998.

16 Buxton RB: The physics of functional magnetic resonance imaging (fMRI). *Reports Prog Phys* 76: 96601, 2013.

17 Cage B, McNeely JH, Russek SE, Halpern HJ: Thermomagnetic properties of the Finland trityl radical. *J Appl Phys* 105: 43905, 2009.

18 Carden DL, Granger DN: Pathophysiology of ischaemia-reperfusion injury. *J Pathol* 190: 255–266, 2000.

19 Carreau A, Hafny-Rahbi B El, Matejuk A, Grillon C, Kieda C: Why is the partial oxygen pressure of human tissues a crucial parameter? Small molecules and hypoxia. *J Cell Mol Med* 15: 1239–1253, 2011.

20 Carver TR, Slichter CP: Experimental Verification of the Overhauser Nuclear Polarization Effect. *Phys Rev* 102: 975–980, 1956.

21 Ceelen W, Smeets P, Backes W, Van Damme N, Boterberg T, Demetter P, Bouckenooghe I, De Visschere M, Peeters M, Pattyn P: Noninvasive monitoring of radiotherapy-induced microvascular changes using dynamic contrast enhanced magnetic resonance imaging (DCE-MRI) in a colorectal tumor model. *Int J Radiat Oncol* 64: 1188–1196, 2006.

22 Coles C, Williams M, Burnet N: Hyperbaric oxygen therapy. Combination with radiotherapy in cancer is of proved benefit but rarely used. *BMJ* 318: 1076-1078, 1999.

23 Couet WR, Brasch RC, Sosnovsky C, Lukszo J, Prakash I, Gnewech CT, Tozer TN: Influerce of chemical structure of nitroxyl spin labels on their reduction by ascorbic acid. *Tetrahedron* 41: 1165–1172, 1985.

24 Dalle-Donne I: Biomarkers of Oxidative Damage in Human Disease. *Clin Chem* 52: 601–623, 2006.

25 Dewhirst MW, Ong ET, Braun RD, Smith B, Klitzman B, Evans SM, Wilson D: Quantification of longitudinal tissue pO2 gradients in window chamber tumours: impact on tumour hypoxia. *Br J Cancer* 79: 1717–1722, 1999.

26 Dhimitruka I, Bobko AA, Eubank TD, Komarov DA, Khramtsov V V: Phosphonated Trityl Probes for Concurrent in Vivo Tissue Oxygen and pH Monitoring Using Electron Paramagnetic Resonance-Based Techniques. *J Am Chem Soc* 135: 5904–5910, 2013.

27 Dhimitruka I, Bobko AA, Hadad CM, Zweier JL, Khramtsov V V: Synthesis and Characterization of Amino Derivatives of Persistent Trityl Radicals as Dual Function pH and Oxygen Paramagnetic Probes. *J Am Chem Soc* 130: 10780–10787, 2008.

28 Dings RPM, Loren M, Heun H, McNiel E, Griffioen AW, Mayo KH, Griffin RJ: Scheduling of Radiation with Angiogenesis Inhibitors Anginex and Avastin Improves Therapeutic Outcome via Vessel Normalization. *Clin Cancer Res* 13: 3395–3402, 2007.

29 Dreher MR, Liu W, Michelich CR, Dewhirst MW, Yuan F, Chilkoti A: Tumor Vascular Permeability, Accumulation, and Penetration of Macromolecular Drug Carriers. *JNCI J Natl Cancer Inst* 98: 335–344, 2006.

30 Dröge W: Free Radicals in the Physiological Control of Cell Function. *Physiol Rev* 82: 47–95, 2002.

31 Eaton SS, Eaton GR: EPR imaging. *J Magn Reson* 59: 474–477, 1984.

32 Efimova O V., Sun Z, Petryakov S, Kesselring E, Caia GL, Johnson D, Zweier JL, Khramtsov V V., Samouilov A: Variable radio frequency proton–electron double-resonance imaging: Application to pH mapping of aqueous samples. *J Magn Reson* 209: 227–232, 2011.

33 Efimova O V, Caia GL, Sun Z, Petryakov S, Kesselring E, Samouilov A, Zweier JL: Standard-based method for proton–electron double resonance imaging of oxygen. *J Magn Reson* 212: 197–203, 2011.

34 Elas M, Williams BB, Parasca A, Mailer C, Pelizzari CA, Lewis MA, River JN, Karczmar GS, Barth ED, Halpern HJ: Quantitative tumor oxymetric images from 4D electron paramagnetic resonance imaging (EPRI): Methodology and comparison with blood oxygen level-dependent (BOLD) MRI. *Magn Reson Med* 49: 682–691, 2003.

35 Epel B, Halpern HJ: In Vivo pO2 Imaging of Tumors. *In*: Methods in enzymology. pp 501–527, 2015.

36 Eto H, Hyodo F, Kosem N, Kobayashi R, Yasukawa K, Nakao M, Kiniwa M, Utsumi H: Redox imaging of

skeletal muscle using in vivo DNP-MRI and its application to an animal model of local inflammation. *Free Radic Biol Med* 89: 1097–1104, 2015.

37 Folkman J: Fundamental Concepts of the Angiogenic Process. *Curr Mol Med* 3: 643–651, 2003.

38 Fujii H, Berliner LJ: One- and two-dimensional EPR imaging studies on Phantoms and Plant specimens. *Magn Reson Med* 2: 275–282, 1985.

39 Gallez B, Mäder K: Accurate and sensitive measurements of pO(2) in vivo using low frequency EPR spectroscopy: how to confer biocompatibility to the oxygen sensors. *Free Radic Biol Med* 29: 1078–1084, 2000.

40 Gallez B, Baudelet C, Jordan BF: Assessment of tumor oxygenation by electron paramagnetic resonance: principles and applications. *NMR Biomed* 17: 240–262, 2004.

41 Gallez B, Jordan BF, Baudelet C, Misson P-D: Pharmacological modifications of the partial pressure of oxygen in murine tumors: Evaluation using in vivo EPR oximetry. *Magn Reson Med* 42: 627–630, 1999.

42 Giaccia: Hypoxic Stress Proteins: Survival of the Fittest. *Semin Radiat Oncol* 6: 46–58, 1996.

43 Gillies RJ, Raghunand N, Garcia-Martin ML, Gatenby RA: pH imaging. A review of pH measurement methods and applications in cancers. *IEEE Eng Med Biol Mag* 23: 57–64.

44 Golman K, Leunbach I, Ardenkjaer-Larsen JH, Ehnholm GJ, Wistrand LG, Petersson JS, Järvi A, Vahasalo S: Overhauser-enhanced MR imaging (OMRI). *Acta Radiol* 39: 10–17, 1998.

45 Golman K, Petersson JS, Ardenkjaer-Larsen JH, Leunbach I, Wistrand LG, Ehnholm G, Liu K: Dynamic in vivo oxymetry using overhauser enhanced MR imaging. *J Magn Reson Imaging* 12: 929–938, 2000.

46 Gomberg M: An Instance Of Trivalent Carbon: Triphenylmethyl. *J Am Chem Soc* 22: 757–771, 1900.

47 Grucker D: In vivo detection of injected free radicals by overhauser effect imaging. *Magn Reson Med* 14: 140–147, 1990.

48 Grucker D, Chambron J: Oxygen imaging in perfused hearts by dynamic nuclear polarization. *Magn Reson Imaging* 11: 691–696, 1993.

49 Grucker D, Guiberteau T, Planinŝic G: Proton-electron double resonance: Spectroscopy and imaging in very low magnetic fields. *Res Chem Intermed* 22: 567–579, 1996.

50 Halpern HJ, Yu C, Peric M, Barth ED, Karczmar GS, River JN, Grdina DJ, Teicher BA: Measurement of Differences in pO 2 in Response to Perfluorocarbon/Carbogen in FSa and NFSa Murine Fibrosarcomas with

Low-Frequency Electron Paramagnetic Resonance Oximetry. *Radiat Res* 145: 610, 1996.

51 Hjortdal VE, Timmenga EJ, Kjølseth D, Brink Henriksen T, Stender Hansen E, Djurhuus JC, Gottrup F: Continuous direct tissue oxygen tension measurement. A new application for an intravascular oxygen sensor. *Ann Chir Gynaecol* 80: 8–13, 1991.

52 Höckel M, Schlenger K, Aral B, Mitze M, Schäffer U, Hockel M, Schlenger K, Aral B, Mitze M, Schaffer U, Vaupel P: Association between tumor hypoxia and malignant progression in advanced cancer of the uterine cervix. *Cancer Res* 56: 4509–4515, 1996.

53 Hockel M, Vaupel P: Tumor Hypoxia: Definitions and Current Clinical, Biologic, and Molecular Aspects. *JNCI J Natl Cancer Inst* 93: 266–276, 2001.

54 Hofer SOP, Timmenga EJF, Christiano R, Bos KE: An intravascular oxygen tension monitoring device used in myocutaneous transplants: A preliminary report. *Microsurgery* 14: 304–309, 1993.

55 Horsman MR, Nordsmark M, Overgaard J: Techniques to assess the oxygenation of human tumors. State of the art. *Strahlenther Onkol* 174 Suppl: 2–5, 1998.

56 Hyodo F, Ito S, Yasukawa K, Kobayashi R, Utsumi H: Simultaneous and Spectroscopic Redox Molecular Imaging of Multiple Free Radical Intermediates Using Dynamic Nuclear Polarization-Magnetic Resonance Imaging. *Anal Chem* 86: 7234–7238, 2014.

57 Hyodo F, Murugesan R, Matsumoto K, Hyodo E, Subramanian S, Mitchell JB, Krishna MC: Monitoring redox-sensitive paramagnetic contrast agent by EPRI, OMRI and MRI. *J Magn Reson* 190: 105–112, 2008.

58 Iannone A, Tomasi A, Vannini V, Swartz HM: Metabolism of nitroxide spin labels in subcellular fractions of rat liver. II. Reduction in the cytosol. *Biochim Biophys Acta* 1034: 290–293, 1990.

59 Iannone A, Tomasi A, Vannini V, Swartz HM: Metabolism of nitroxide spin labels in subcellular fraction of rat liver. I. Reduction by microsomes. *Biochim Biophys Acta* 1034: 285–289, 1990.

60 Ichiwata T, Sasao G, Abe T, Kikuchi K, Koyama K, Fujiwara H, Nagai A, Kuwahira I, Nagao K: Oxidative capacity of the skeletal muscle and lactic acid kinetics during exercise in healthy subjects and patients with COPD. *Adv Exp Med Biol* 662: 537–543, 2010.

61 Jain RK: Lessons from multidisciplinary translational trials on anti-angiogenic therapy of cancer. *Nat Rev Cancer* 8: 309–316, 2008.

62 Jain RK: Molecular regulation of vessel maturation. *Nat Med* 9: 685–693, 2003.

63 Jain RK: Normalizing tumor vasculature with anti-angiogenic therapy: a new paradigm for combination therapy. *Nat Med* 7: 987–989, 2001.

64 Jenner P: Oxidative stress in Parkinson's disease. *Ann Neurol* 53: S26–S38, 2003.

65 Kaiser R: Use of the Nuclear Overhauser Effect in the Analysis of High-Resolution Nuclear Magnetic Resonance Spectra. *J Chem Phys* 39: 2435–2442, 1963.

66 Kashiwagi S, Tsukada K, Xu L, Miyazaki J, Kozin S V, Tyrrell JA, Sessa WC, Gerweck LE, Jain RK, Fukumura D: Perivascular nitric oxide gradients normalize tumor vasculature. *Nat Med* 14: 255–7, 2008.

67 Khan N, Williams BB, Hou H, Li H, Swartz HM: Repetitive Tissue pO 2 Measurements by Electron Paramagnetic Resonance Oximetry: Current Status and Future Potential for Experimental and Clinical Studies. *Antioxid Redox Signal* 9: 1169–1182, 2007.

68 Khramtsov V V., Bobko AA, Tseytlin M, Driesschaert B: Exchange Phenomena in the Electron Paramagnetic Resonance Spectra of the Nitroxyl and Trityl Radicals: Multifunctional Spectroscopy and Imaging of Local Chemical Microenvironment. *Anal Chem* 89: 4758–4771, 2017.

69 Khramtsov V V., Caia GL, Shet K, Kesselring E, Petryakov S, Zweier JL, Samouilov A: Variable Field Proton–Electron Double-Resonance Imaging: Application to pH mapping of aqueous samples. *J Magn Reson* 202: 267–273, 2010.

70 Khramtsov V V, Grigor'ev IA, Foster MA, Lurie DJ, Nicholson I: Biological applications of spin pH probes. *Cell Mol Biol (Noisy-le-grand)* 46: 1361–1374, 2000.

71 Kinoshita Y, Yamada K-I, Yamasaki T, Sadasue H, Sakai K, Utsumi H: Development of novel nitroxyl radicals for controlling reactivity with ascorbic acid. *Free Radic Res* 43: 565–571, 2009.

72 Kosem N, Naganuma T, Ichikawa K, Phumala Morales N, Yasukawa K, Hyodo F, Yamada K, Utsumi H: Whole-body kinetic image of a redox probe in mice using Overhauser-enhanced MRI. *Free Radic Biol Med* 53: 328–336, 2012.

73 Kraig RP, Petito CK, Plum F, Pulsinelli WA: Hydrogen Ions Kill Brain at Concentrations Reached in Ischemia. *J Cereb Blood Flow Metab* 7: 379–386, 1987.

74 Kraut JA, Madias NE: Consequences and therapy of the metabolic acidosis of chronic kidney disease. *Pediatr Nephrol* 26: 19–28, 2011.

75 Krishna MC, English S, Yamada K, Yoo J, Murugesan R, Devasahayam N, Cook JA, Golman K,

Ardenkjaer-Larsen JH, Subramanian S, Mitchell JB: Overhauser enhanced magnetic resonance imaging for tumor oximetry: Coregistration of tumor anatomy and tissue oxygen concentration. *Proc Natl Acad Sci* 99: 2216–2221, 2002.

76 Krishna MC, Russo A, Mitchell JB, Goldstein S, Dafni H, Samuni A: Do nitroxide antioxidants act as scavengers of O2-. or as SOD mimics? *J Biol Chem* 271: 26026–26031, 1996.

77 Lagrota-Candido J, Canella I, Pinheiro DF, Santos-Silva LP, Ferreira RS, Guimarães-Joca FJ, Lannes-Vieira J, Quirico-Santos T: Characteristic pattern of skeletal muscle remodelling in different mouse strains. *Int J Exp Pathol* 91: 522–529, 2010.

78 Lurie DJ: Progress toward whole-body proton—electron double-resonance imaging of free radicals. *Magma Magn Reson Mater Physics, Biol Med* 2: 267–271, 1994.

79 Lurie DJ, Bussell DM, Bell LH, Mallard JR: Proton-electron double magnetic resonance imaging of free radical solutions. *J Magn Reson* 76: 366–370, 1988.

80 Lurie DJ, Davies GR, Foster MA, Hutchison JMS: Field-cycled PEDRI imaging of free radicals with detection at 450 mT. *Magn Reson Imaging* 23: 175–181, 2005.

81 Lurie DJ, Hutchison JM., Bell LH, Nicholson I, Bussell DM, Mallard JR: Field-cycled proton-electron double-resonance imaging of free radicals in large aqueous samples. *J Magn Reson* 84: 431–437, 1989.

82 Lurie DJ, Li H, Petryakov S, Zweier JL: Development of a PEDRI free-radical imager using a 0.38 T clinical MRI system. *Magn Reson Med* 47: 181–186, 2002.

83 Lurie DJ, Foster MA, Yeung D, Hutchison JMS: Design, construction and use of a large-sample field-cycled PEDRI imager. *Phys Med Biol* 43: 1877–1886, 1998.

84 Mallard JR, Kent M: Electron Spin Resonance in Surviving Rat Tissues. *Nature* 210: 588–591, 1966.

85 Maltempo MM, Eaton SS, Eaton GR: Spectral-spatial two-dimensional EPR imaging. *J Magn Reson* 72: 449–455, 1987.

86 Maritim AC, Sanders RA, Watkins JB: Diabetes, oxidative stress, and antioxidants: A review. *J Biochem Mol Toxicol* 17: 24–38, 2003.

87 Markesbery WR: Oxidative Stress Hypothesis in Alzheimer's Disease. *Free Radic Biol Med* 23: 134–147, 1997.

88 Mason RP, Jeffrey FMH, Malloy CR, Babcock EE, Antich PP: A noninvasive assessment of myocardial

oxygen tension:19F NMR spectroscopy of sequestered perfluorocarbon emulsion. *Magn Reson Med* 27: 310–317, 1992.

89 Mateescu GD, Cabrera ME: In vivo 17O magnetic resonance spectroscopy. Determination of temperature effects on metabolic rates (Q10 factor). *Adv Exp Med Biol* 411: 585–590, 1997.

90 Matsumoto K, Hyodo F, Anzai K, Utsumi H, Mitchell JB, Krishna MC: Brain Redox Imaging. *In*: Methods in molecular biology (Clifton, N.J.). pp 397–419, 2011.

91 Matsumoto S, Yasui H, Batra S, Kinoshita Y, Bernardo M, Munasinghe JP, Utsumi H, Choudhuri R, Devasahayam N, Subramanian S, Mitchell JB, Krishna MC: Simultaneous imaging of tumor oxygenation and microvascular permeability using Overhauser enhanced MRI. *Proc Natl Acad Sci* 106: 17898–17903, 2009.

92 Matsumoto S, Hyodo F, Subramanian S, Devasahayam N, Munasinghe J, Hyodo E, Gadisetti C, Cook JA, Mitchell JB, Krishna MC: Low-field paramagnetic resonance imaging of tumor oxygenation and glycolytic activity in mice. *J Clin Invest* 118: 1965–1973, 2008.

93 Matsumoto S, Utsumi H, Aravalluvan T, Matsumoto K-I, Matsumoto A, Devasahayam N, Sowers AL, Mitchell JB, Subramanian S, Krishna MC: Influence of proton T1 on oxymetry using Overhauser enhanced magnetic resonance imaging. *Magn Reson Med* 54: 213–217, 2005.

94 Maxwell PH, Dachs GU, Gleadle JM, Nicholls LG, Harris AL, Stratford IJ, Hankinson O, Pugh CW, Ratcliffe PJ: Hypoxia-inducible factor-1 modulates gene expression in solid tumors and influences both angiogenesis and tumor growth. *Proc Natl Acad Sci U S A* 94: 8104–8109, 1997.

95 Naumov GN, Akslen LA, Folkman J: Role of Angiogenesis in Human Tumor Dormancy: Animal Models of the Angiogenic Switch. *Cell Cycle* 5: 1779–1787, 2006.

96 Ndubuizu O, LaManna JC: Brain Tissue Oxygen Concentration Measurements. *Antioxid Redox Signal* 9: 1207–1220, 2007.

97 Neveu M-A, Joudiou N, De Preter G, Dehoux J-P, Jordan BF, Gallez B: ^{17}O MRS assesses the effect of mild hypothermia on oxygen consumption rate in tumors. *NMR Biomed* 30: e3726, 2017.

98 Niwano S, Tojo T: Systemic acidosis in acute myocardial ischemia--cause or result of life-threateningventricular arrhythmia? *Circ J* 74: 1794–1795, 2010.

99 Noseworthy MD, Bulte DP, Alfonsi J: BOLD Magnetic Resonance Imaging of Skeletal Muscle. *Semin*

Musculoskelet Radiol 7: 307–316, 2003.

100 Overhauser AW: Polarization of Nuclei in Metals. *Phys Rev* 92: 411–415, 1953.

101 Parhami P, Fung BM: Fluorine-19 relaxation study of perfluoro chemicals as oxygen carriers. *J Phys Chem* 87: 1928–1931, 1983.

102 Potapenko DI, Foster MA, Lurie DJ, Kirilyuk IA, Hutchison JMS, Grigor'ev IA, Bagryanskaya EG, Khramtsov V V: Real-time monitoring of drug-induced changes in the stomach acidity of living rats using improved pH-sensitive nitroxides and low-field EPR techniques. *J Magn Reson* 182: 1–11, 2006.

103 Quintanilha AT, Packer L: Surface localization of sites of reduction of nitroxide spin-labeled molecules in mitochondria. *Proc Natl Acad Sci U S A* 74: 570–574, 1977.

104 Rasey JS, Koh WJ, Evans ML, Peterson LM, Lewellen TK, Graham MM, Krohn KA: Quantifying regional hypoxia in human tumors with positron emission tomography of [18F]fluoromisonidazole: a pretherapy study of 37 patients. *Int J Radiat Oncol Biol Phys* 36: 417–428, 1996.

105 Reddy TJ, Iwama T, Halpern HJ, Rawal VH: General Synthesis of Persistent Trityl Radicals for EPR Imaging of Biological Systems. *J Org Chem* 67: 4635–4639, 2002.

106 Ribeiro PD, Sanches MG, Okamoto T: Comparative analysis of tissue reactions to anesthetic solutions: histological analysis in subcutaneous tissue of rats. *Anesth Prog* 50: 169–80, 2003.

107 Robinson SP, Griffiths JR: Current issues in the utility of 19F nuclear magnetic resonance methodologies for the assessment of tumour hypoxia. *Philos Trans R Soc B Biol Sci* 359: 987–996, 2004.

108 Samouilov A, Efimova O V, Bobko AA, Sun Z, Petryakov S, Eubank TD, Trofimov DG, Kirilyuk IA, Grigor'ev IA, Takahashi W, Zweier JL, Khramtsov V V: In Vivo Proton–Electron Double-Resonance Imaging of Extracellular Tumor pH Using an Advanced Nitroxide Probe. *Anal Chem* 86: 1045–1052, 2014.

109 Sano H, Naruse M, Matsumoto K, Oi T, Utsumi H: A new nitroxyl-probe with high retention in the brain and its application for brain imaging. *Free Radic Biol Med* 28: 959–969, 2000.

110 Schwarz PF, Turro NJ, Bossmann SH, Braun AM, Wahab A-MAA, Dürr H: A New Method To Determine the Generation of Hydroxyl Radicals in Illuminated TiO 2 Suspensions. *J Phys Chem B* 101: 7127–7134, 1997.

111 Seimenis I, Foster MA, Lurie DJ, Hutchison JMS, Whiting PH, Payne S: The excretion mechanism of the spin label proxyl carboxylic acid (PCA) from the rat monitored by X-band ESR and PEDRI. *Magn Reson*

Med 37: 552–558, 1997.

112 Shiba T, Yamato M, Kudo W, Watanabe T, Utsumi H, Yamada K: In vivo imaging of mitochondrial function in methamphetamine-treated rats. *Neuroimage* 57: 866–872, 2011.

113 Singh U, Jialal I: Oxidative stress and atherosclerosis. *Pathophysiology* 13: 129–142, 2006.

114 Spasojević I: Electron Paramagnetic Resonance - A Powerful Tool of Medical Biochemistry in Discovering Mechanisms of Disease and Treatment Prospects. *J Med Biochem* 29, 2010.

115 Stratford IJ, Adams GE, Bremner JC, Cole S, Edwards HS, Robertson N, Wood PJ: Manipulation and exploitation of the tumour environment for therapeutic benefit. *Int J Radiat Biol* 65: 85–94, 1994.

116 Su MY, Mühler A, Lao X, Nalcioglu O: Tumor characterization with dynamic contrast-enhanced MRI using MR contrast agents of various molecular weights. *Magn Reson Med* 39: 259–269, 1998.

117 Subczynski WK, Lukiewicz S, Hyde JS: Murine in vivo L-band ESR spin-label oximetry with a loop-gap resonator. *Magn Reson Med* 3: 747–754, 1986.

118 Subramanian S, Matsumoto K-I, Mitchell JB, Krishna MC: Radio frequency continuous-wave and time-domain EPR imaging and Overhauser-enhanced magnetic resonance imaging of small animals: instrumental developments and comparison of relative merits for functional imaging. *NMR Biomed* 17: 263–294, 2004.

119 Sven Andersson, Finn Radner, Anna Rydbeek, Rolf Servin, Lars-Goran Wistrand: US5530140A - US Patents., 1996.

120 Swartz HM, Clarkson RB: The measurement of oxygen in vivo using EPR techniques. *Phys Med Biol* 43: 1957–75, 1998.

121 Swartz HM, Sentjurc M, Morse PD: Cellular metabolism of water-soluble nitroxides: Effect on rate of reduction of cell/nitroxide ratio, oxygen concentrations and permeability of nitroxides. *Biochim Biophys Acta - Mol Cell Res* 888: 82–90, 1986.

122 Takahashi W, Bobko AA, Dhimitruka I, Hirata H, Zweier JL, Samouilov A, Khramtsov V V.: Proton-Electron Double-Resonance Imaging of pH Using Phosphonated Trityl Probe. *Appl Magn Reson* 45: 817–826, 2014.

123 Utsumi H, Shimakura A, Kashiwagi M, Hamada A: Localization of the active center of nitroxide radical reduction in rat liver microsomes: its relation to cytochrome P-450 and membrane fluidity. *J Biochem* 105: 239–244, 1989.

124 Utsumi H, Hyodo F: Free Radical Imaging Using In Vivo Dynamic Nuclear Polarization-MRI. *In*: Methods in Enzymology. 1st ed. Elsevier Inc., pp 553–571, 2015.

125 Utsumi H, Yamada K -i., Ichikawa K, Sakai K, Kinoshita Y, Matsumoto S, Nagai M: Simultaneous molecular imaging of redox reactions monitored by Overhauser-enhanced MRI with 14N- and 15N-labeled nitroxyl radicals. *Proc Natl Acad Sci* 103: 1463–1468, 2006.

126 Vaupel P: Oxygenation status of malignant tumors: Pathogenesis of hypoxia and significance for tumor therapy. *Semin Oncol* 28: 29–35, 2001.

127 Vaupel P, Schlenger K, Hoeckel M: Blood Flow and Tissue Oxygenation of Human Tumors: An Update. *In*: Oxygen Transport to Tissue XIV. Springer US, pp 139–151, 1992.

128 Velan SS, Spencer RG, Zweier JL, Kuppusamy P: Electron paramagnetic resonance oxygen mapping (EPROM): direct visualization of oxygen concentration in tissue. *Magn Reson Med* 43: 804–809, 2000.

129 Voest EE, van Faassen E, Marx JJ: An electron paramagnetic resonance study of the antioxidant properties of the nitroxide free radical TEMPO. *Free Radic Biol Med* 15: 589–595, 1993.

130 Wagner K, Bossen W, Schramm U: Tissue Alterations by the Penetration of a PO2 Sensing Needle Probe. *In*: Oxygen Transport to Tissue XIV. Springer US, pp 639–644, 1992.

131 Williams BB, al Hallaq H, Chandramouli GVR, Barth ED, Rivers JN, Lewis M, Galtsev VE, Karczmar GS, Halpern HJ: Imaging spin probe distribution in the tumor of a living mouse with 250 MHz EPR: Correlation with BOLD MRI. *Magn Reson Med* 47: 634–638, 2002.

132 Woitzik J, Back T, Thome C: Flow-dependent versus spreading-like impairment of brain tissue integrity during focal cerebral ischemia and its consequences for neuroprotective strategies. *Front Biosci* 13: 1500–1506, 2008.

133 Yamato M, Shiba T, Naganuma T, Ichikawa K, Utsumi H, Yamada K: Overhauser-enhanced magnetic resonance imaging characterization of mitochondria functional changes in the 6-hydroxydopamine rat model. *Neurochem Int* 59: 804–811, 2011.

134 Yong L, Harbridge J, Quine RW, Rinard GA, Eaton SS, Eaton GR, Mailer C, Barth E, Halpern HJ: Electron Spin Relaxation of Triarylmethyl Radicals in Fluid Solution. *J Magn Reson* 152: 156–161, 2001.

135 Zhang X, Lin Y, Gillies RJ: Tumor pH and its measurement. *J Nucl Med* 51: 1167–1170, 2010.

136 Zhu X-H, Zhang Y, Wiesner HM, Ugurbil K, Chen W: In vivo measurement of CBF using ^{17}O NMR signal

of metabolically produced $H_2{}^{17}O$ as a perfusion tracer. *Magn Reson Med* 70: 309–314, 2013.

137 Zweier JL, Thompson-Gorman S, Kuppusamy P: Measurement of oxygen concentrations in the intact beating heart using electron paramagnetic resonance spectroscopy: a technique for measuring oxygen concentrations in situ. *J Bioenerg Biomembr* 23: 855–871, 1991.